SAND76-0086
Unlimited Release

Drilling Research on the Electrical Detonation and Subsequent Cavitation in a Liquid Technique (Spark Drilling)

Status Report July 1 - December 31, 1975

Drilling Research Division

Prepared by Sandia Laboratories, Albuquerque, New Mexico 87115 and Livermore, California 94550 for the United States Energy Research and Development Administration under Contract AT(29-1)-789

Printed April 1976

When printing a copy of any digitized SAND Report, you are required to update the markings to current standards.

Sandia Laboratories
energy report

Issued by Sandia Laboratories, operated for the United States Energy Research and Development Administration by Sandia Corporation.

NOTICE

This report was prepared as an account of work sponsored by the United States Government. Neither the United States nor the United States Energy Research and Development Administration, nor any of their employees, nor any of their contractors, subcontractors, or their employees, makes any warranty, express or implied, or assumes any legal liability or responsibility for the accuracy, completeness or usefulness of any information, apparatus, product or process disclosed, or represents that its use would not infringe privately owned rights.

SAND76-0086
Unlimited Release
Printed April 1976

DRILLING RESEARCH ON THE ELECTRICAL DETONATION AND SUBSEQUENT CAVITATION IN A LIQUID TECHNIQUE (SPARK DRILLING)

STATUS REPORT

JULY 1 - DECEMBER 31, 1975

Drilling Research Division - 5718
Sandia Laboratories, Albuquerque, NM 87115

ABSTRACT

The electrical characteristics of water during a rapid electrical discharge have been determined. These characteristics were used in predicting energy in the spark drilling arc and in designing a new-generation spark drill. The design of this drill system is described, along with the proposed schedule of its fabrication and use. Other activities accomplished during this report period are also discussed.

Approved by: M. M. Newsom - Principal Investigator

MEDIA - ENVIRONMENTAL REPORTERS

1. Don Thompson, Industry Week Magazine
2. Ted Blankenship, Wichita Eagle
3. Joe Matula, Gulf Oil Magazine
4. Colin Leinster, Free-Lance Writer, NYC
5. Hal Scott, Florida Audubon Society
6. Harold N. Scarlett, Houston Post
7. Peter G. Miller, Republic News Service, Wash., DC
8. Ralph Hallow, Pittsburgh Post Dispatch
9. Hiram S. McDonald, Deseret News, Salt Lake City
10. Doris Nieh, Free-Lance Writer, LA
11. Norman Sklarewitz, Free-Lance Writer, San Francisco
12. Don Harris, Dallas Morning News
13. Ralph Wennblom, Farm Journal
14. Sam Fox, Tulsa Tribune
15. Tom Turner, Friends of the Earth
16. Patricia Sarr, Friends of the Earth (Camera)
17. Doris Johnson, Louisville Defender
18. Ethel Payne, Chicago Defender
19. James Cassell, Philadelphia Tribune
20. Charles Belle, San Francisco Sun Reporter
21. Herb Karner, Tulsa World
22. Joe Isakson, The Farmer
23. Gerald Bradley, Gulf Oil
24. Thomas Walker, Gulf Oil
25. S. S. Zippay, J. I. Gatten, Donald Pratt, John Allen, Mary Stoll (Camera) - Gulf Oil
26. W. R. Zarrella, World Wide Gulf Oil Environmental Coordinator

CONTENTS

	Page
MEDIA - ENVIRONMENTAL REPORTERS	4
HIGHLIGHTS AND SUMMARY	7
PAPERS AND MAJOR PRESENTATIONS	8
BRIEFINGS	8
Chapter 1 - INTRODUCTION	9
Chapter 2 - ELECTRICAL CHARACTERISTICS OF DRILLING FLUID DURING SPARK DISCHARGE	10
Electrical Impedance, Breakdown Voltage, Delay Time, and Channel Formation	10
Summary	10
The Discharge Circuit	10
Voltage-Current Waveforms	12
Results	13
Conclusions	19
Electrical Energy Input to the Spark Channel	19
Summary	19
Discussion	19
Spark-Generated Environment - Pressure Measurement	23
Energy Density of the Channel	25
Chapter 3 - DYNAMICS OF A SPARK-GENERATED BUBBLE IN A HIGH-PRESSURE FLUID	26
Summary	26
Discussion	26
Chapter 4 - HIGH-ENERGY SPARK DRILL SYSTEMS	28
Summary	28
Desired Design Characteristics	28
Design Approach	29
Design and Fabrication Status	33
Chapter 5 - SPARK DRILLING EXPERIMENTS	34
Summary	34
Ejecta Experiments	34
Indiana Limestone and Berea Sandstone	34
Effect of Fluid Jet on Spark Drilling Phenomena	37
Bit Experiments	37
Chapter 6 - ROCK-FRACTURE INVESTIGATIONS	39
Summary	39
Discussion	39
Chapter 7 - MULTIPURPOSE ENVIRONMENTAL TEST SYSTEM	43
Summary	43
Discussion	44

CONTENTS (cont)

	Page
Chapter 8 - MAJOR LABORATORY EQUIPMENT ADDITIONS	48
Rock Saw	48
Pressure Pump	48
Chapter 9 - FACILITIES	49
References	50

FIGURES

Figure		Page
1	Electrical Circuit Schematic	11
2	Tube and Electrode Assembly	12
3	Voltage and Current Waveforms as Recorded and After Correction for Reactance	13
4	Channel Impedance During Breakdown	14
5	Resistance of Arc Channel in Formative Stage. Iron Electrodes 0.159 cm Diameter Spaced 1.01 cm Apart	15
6	Voltage Required for Prompt Breakdown in Distilled Water	16
7	Delay Time to Breakdown With 3-cm Electrode Spacing	17
8	Electrical Resistance of an Arc in Tap Water	17
9	Energy and Breakdown Voltage vs Electrode Gap Spacing for a Typical Bit Configuration	17
10	Simplified Circuit Diagram of Pulse Generator	30
11	Pulse Generator Assembly	30
12	Rotary Switch - Side View	32
13	Rotary Switch - Top View	32
14	Exposed Electrode Bit	32
15	Present Laboratory Drill System	35
16	Present Laboratory Drill Bit and Experiment Chamber	35
17	Types of Rock Fracture	36
18	Conical Bit Design	38
19	Conical Bit After Test	38
20	Exposed Electrode Bit	38
21	Failure Envelope for Indiana Limestone	40
22	Failure Envelope for Berea Sandstone	40
23	Typical Erosion Characteristics of Material	40
24	Typical Shear Strength vs Compression Stress	41
25	Diagram of Two-Dimensional Stress Problem	41
26	Environmental Test Vessel	46
27	Sapphire Window	46
28	Quarter-Scale Vessel Instrumentation Feedthrough	47
29	Quarter-Scale Environmental Test Vessel	47

HIGHLIGHTS AND SUMMARY

Experimental data on the electrical characteristics of fluids have been generated for a rapid electrical discharge. This basically is new information which has not appeared in the published technical literature. A mathematical formula has been developed to predict the energy deposited in the arc and has been shown, by the use of the above data, to be more accurate than previously published results.

The experimental results verify that a spark drill must have characteristics which include high voltage, a large voltage-to-inductance ratio, and high spark energies. As a result the design of a spark generator having these characteristics has been completed and its fabrication is approximately 50 percent complete. Even though the total power is lower than desired, we believe the quality of the spark will be sufficient to generate drilling data that can be used in predicting the economics and feasibility of the spark drill concept.

In brief, a considerable amount of data has been acquired during this report period and the groundwork is now being laid for application of this information to a large spark generator in the near future.

PAPERS AND MAJOR PRESENTATIONS

Alvis, R. L. and Huff, C. F., "Advanced Drilling Research - Some Materials Needs, Problems, and Potential," 7th National SAMPE Technical Conference, (October 14-16, 1975), Albuquerque, NM.

Alvis, R. L. and Milton, O., "The Practicability of Drilling With Underwater Sparks," 7th National SAMPE Technical Conference, (October 14-16, 1975), Albuquerque, NM.

Huff, C. F. and Graham, R. A., "Pressure Measurements Very Near an Electrical Arc Discharge in a Liquid Using a Lithium Niobate Piezoelectric Transducer," Applied Physics Letters, Vol. 27, No. 4 (August 15, 1975), pp 163-164 and the Pasadena Meeting of the American Physical Society (December 29-31, 1975).

Lawrence, R. J. and Young, E. G., Numerical Analysis of Spark Drill Phenomenology, Sandia Laboratories SAND75-0501 (October 1975).

Newsom, M. M. and Friedman, M., "Spark Drilling," ASME-Petroleum Division Meeting, Tulsa, OK, (September 24, 1975).

Newsom, M. M. and Alvis, R. L., "Advanced Drilling Systems," Sandia Laboratories Technical Review.

BRIEFINGS

Bert Shapiro	Connecticut Public Television	8-19-75
Lawrence Bell	ERDA, Div. of Geothermal Energy	9-17-75
M. B. Skalka	ERDA, Div. of Geothermal Energy	9-17-75
Ronald S. H. Toms	ERDA, Div. of Geothermal Energy	9-17-75
Don Martin	Energy Resarch Reports	9-18-75
R. F. Evans	Smith Tool Company	10-8-75
Walter Liljestrand	Drilco - Oilfield	10-8-75
W. F. Olson	Drilco Industrial	10-8-75
Royce Calloway	Drilco - Oilfield	10-8-75
Stanley C. Moore	Smith International	10-8-75
Albert Ellis	Univ. of Cal., San Diego	10-22-75
Tom Aiken	ERDA, Asst. Dir. of Administration for Geothermal	10-24-75
Al Schernoff	ERDA-ALO	10-24-75
James F. Murray	G. E. Carboloy	11-5-75
Arnold B. Bower	G. E. Carboloy	11-5-75
Joseph A. Martin	G. E. Carboloy	11-5-75
Mahlon D. Dennis	G. E. Material Research	11-5-75
Israel Energy Repr.	Israel Government	11-20-75
Tom Dau	Western Electric	12-7-75
ERDA Geothermal	ERDA Washington	12-9-75

Chapter 1

INTRODUCTION

Sandia's spark drilling status report dated July 1975 presented the spark drill concept, results of preliminary drilling experiments, and areas which needed further investigation. This report presents a continuation of these efforts to January 1, 1976.

As can be seen in this report, considerable attention has been given to the basic principles involved in electrical discharges in a fluid environment and to the resulting phenomena. This work has led to a better understanding of the key system parameters in an improved laboratory spark drill system that are being incorporated into a new experimental system. With the new system we expect to obtain data from which we can extrapolate to an operational spark drilling system. This information will be used to judge the feasibility of the drilling concept.

The new laboratory drilling system should be in operation by April 1, 1976, and drilling results achieved by July 1, 1976. Although compromises have been made in some areas of the design to save money and to meet this schedule, none should affect the quality of the results.*

The information in this report is presented in both a summarized and a detailed manner for the convenience of the reader.

---

*Editors Note: At the time that this report was written it was anticipated that the FY 76 funding level for the spark drill research program would be near the requested level, and milestone schedules were based on this assumption. Since the higher funding levels have not been approved by ERDA/Division of Geothermal Energy, key dates in this report should be slipped approximately 6 months.

Chapter 2

ELECTRICAL CHARACTERISTICS OF DRILLING FLUID DURING SPARK DISCHARGE

Electrical Impedance, Breakdown Voltage, Delay Time, and Channel Formation

Summary

The channel impedance was determined as a function of time for water during an electrical discharge. It showed that the gap impedance changes in value by several orders of magnitude in a period of 2 to 3 ns, holds steady for a short period of time, then falls into the milliohm range. Other drilling fluids tested showed similar results. Delay periods between the time that voltage was applied to the electrodes and the time that gap breakdown occurred were observed, and the longer delays were shown to be detrimental to shock wave formation. These results indicate that an efficient spark drill system must have (1) system impedance in the milliohm range, (2) high voltage to minimize breakdown delay and allow wider electrode gap spacing, and (3) a high voltage to generate strong shock waves. These characteristics are being incorporated into the design of a new spark drill system.

Knowledge of the electrical impedance of a spark channel in water is necessary for designing a generating system which will have the proper storage capability and best practical output impedance for optimum energy transfer to the drilling liquid. Data on spark channel impedance in water have been published; for example, E. A. Martin has given results from an underwater discharge of energy stored in 25-kV capacitors.[1] Our work, however, has shown that the spark channel develops in nanoseconds and that significant changes in spark impedance occur in a fraction of a microsecond. We are not attempting to define spark and arc here, but we assume that the spark has occurred before equilibrium and before an arc has formed.

The Discharge Circuit

Two types of discharge circuits were used in this investigation. One, similar to that used by Martin, is a circuit wherein an energy storage capacitor is discharged by a gaseous spark gap to the electrodes in water.[1] Voltages up to 50 kV are applied but, since the triggered spark gap is close to the capacitor and inductance in the line from the gap to the spark electrodes is about 1.6 μH, the current-rise rate is slowed by the large L/R ratio. Nevertheless, this circuit is representative of possible generator designs and is useful for examining shock pressures, delay times at low voltage, electrode geometry, and insulation problems that may be significant with prototype generators. A further advantage is that large amounts (kilojoules) of stored energy may be easily obtained. Data are recorded with a bandwidth of 50 MHz.

The other system is a high-speed circuit at higher voltage, where the energy from the storage capacitor is passed to a transformer which steps up the voltage and charges a pulse-forming coaxial line. A fast-breakdown, high-pressure (SF_6 gas) self-firing switch at the end of the charged line shorts the line to a low-inductance electrode assembly. The schematic of this circuit is shown in Figure 1. The characteristic impedance of the line is 10 Ω; stored in the line are 70 to 170 J, depending on charge voltage before switching. Voltages in the neighborhood of 500 kV are typical.

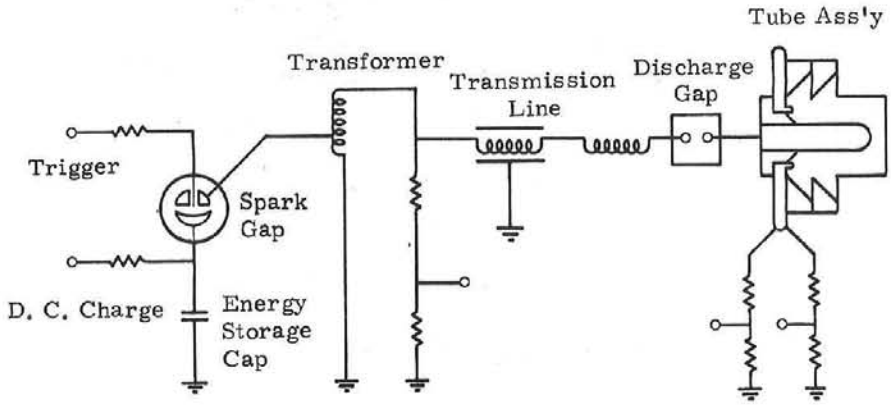

Figure 1. Electrical Circuit Schematic

Risetime of the current is governed by the electrical characteristics of the spark and by the inductance of the tube assembly and the electrodes. Short circuit tests showed the tube inductance to be 70 nH, and the electrode inductance to be 50 nH for 3-mm-diameter electrodes. A cross-section view of the tube assembly with the water test cell is shown in Figure 2. Before voltage is applied, the tube assembly is filled with SF_6 at a pressure of 28 kPa to prevent surface discharge on the test cell. Each discharge is photographed to determine that a single arc channel is formed between electrode ends before accepting the data because it is not always possible to tell from the oscilloscope readings whether multiple channels have formed. The location of voltage and current probes are shown in Figure 2. Voltage and current waveforms are obtained at close distance to the spark in order to reduce undesired reactance effects on the waveforms. These waveforms are correlated to additional waveforms obtained about 100 mm away from the arc. A bandwidth of greater than 500 MHz is used in the electrical recordings. The voltage and current waveforms are time correlated to within 1 ns by means of a 2-ns-wide fiducial mark on each recording. All transmission lines are matched with a time-domain reflectometer and terminated in their characteristic impedance.

Experiments were conducted by using tap water, drilling mud, and distilled and deionized water of low conductance.

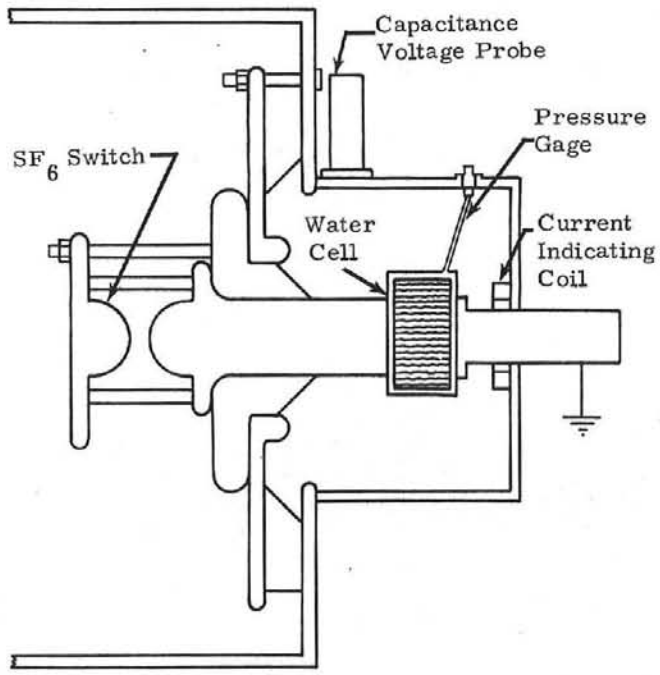

Figure 2. Tube and Electrode Assembly

Voltage-Current Waveforms

Typical voltage and current waveforms are shown in Figure 3. The voltage waveform close to the electrode gap rises to 500 kV in about 16 ns. The capacitance probe used to measure voltage works into a 50 Ω terminated line and has a time constant of 60 ns; hence, as shown on the figure, a small correction is required from the waveform to account for lost charge. When breakdown occurs between electrodes, the voltage drops suddenly but the capacitance probe is slightly high with respect to the gap because of inductance from the spark to the viewing area on the cathode shank. Consequently, damped oscillations occur because of reactance in the electrode-tube circuit. The voltage waveform, corrected for leakage from the capacitance probe and the reactance from the electrode shank, is shown as a dashed line.

The current rises with the voltage before breakdown occurs. The initial rise in current is the sum of two components: One is conduction (i.e., loss) current; the other, a charging (C dv/dt) current for the electrode capacitance. Because of the high dielectric constant of water, careful electrode placement is required for minimizing the C dv/dt current. With the drop in voltage, an initial very rapid rise in current is detected, followed by a pause in current rise. It has been proposed that the pause in current is due to inertia in channel expansion.[2] Another explanation

might be that it is a consequence of local charge (on the electrodes) delivered at low inductance, which is now exhausted. E. A. Martin used initiating wires for the spark and attributed the pause in current to the moment at which the wire vaporized.[1] After the current pause, the main current from the pulse-forming line rises with its L/R time constant, as shown in Figure 3.

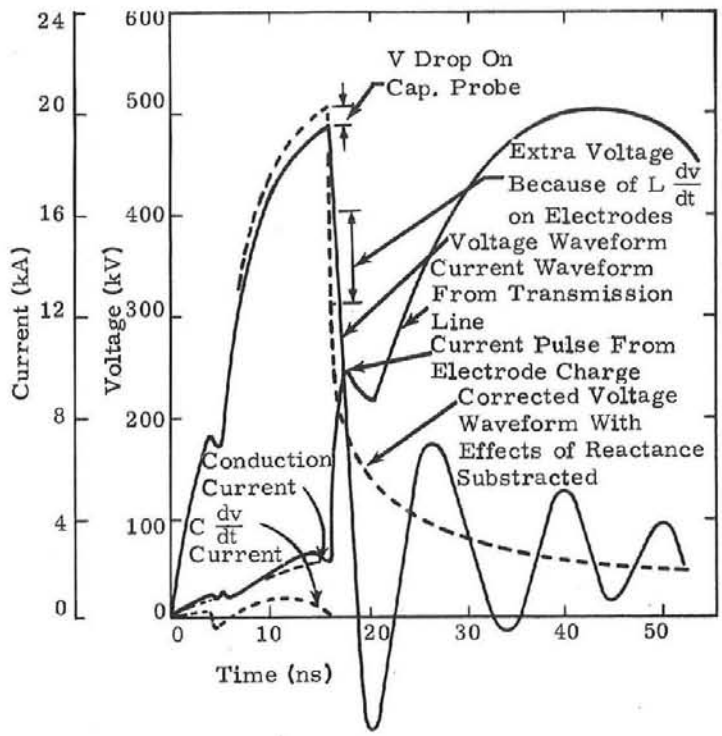

Figure 3. Voltage and Current Waveforms as Recorded and After Correction for Reactance

Results

A curve showing electrical impedance and resistance as the channel forms in distilled water is given in Figure 4. The purpose of Figure 4 is to illustrate the difference between the impedance and the resistance as a function of time and is not necessarily typical of all sparks in water. Therefore, the impedance, which is several hundred ohms because of conduction current and C dv/dt current occurring before breakdown, is not shown on this curve. The resistance curve is the important curve for spark drill design because it is determined by energy input to the spark, whereas the impedance curve includes reactance effects from stray or unwanted inductance not directly related to the spark energy. The fall time of the spark channel resistance, shown here as 2-3 ns, may be increased slightly if the gap length is increased. The magnitude of the resistance in the toe can be increased appreciably if the gap length is increased. It is most significant (and typical) that as the channel forms the voltage falls rapidly, resulting in a large difference in the

instantaneous magnitude of impedance and resistance. Another result is a toe in the curve, where the resistance holds more than an ohm for a period of time.

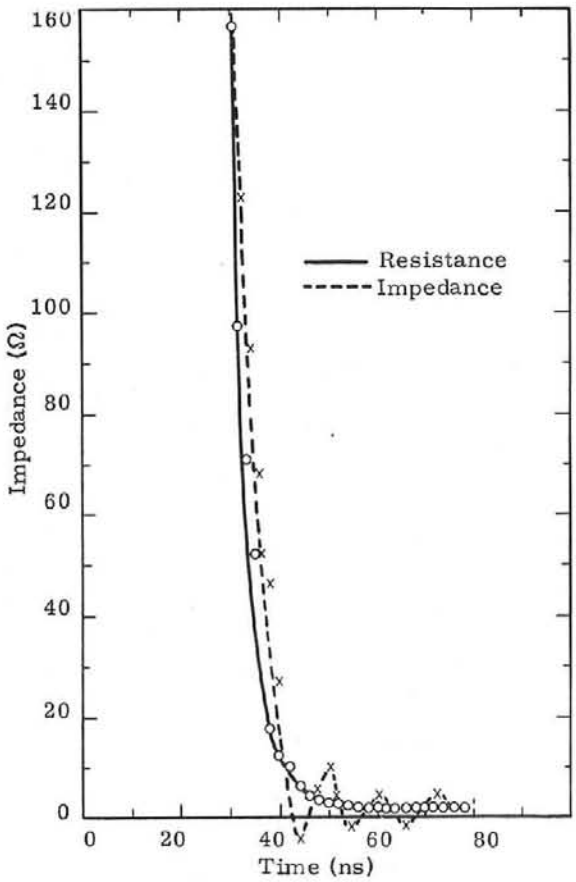

Figure 4. Channel Impedance During Breakdown

Figure 5 shows the resistance of the arc channel in dirty tap water. The resistance (1000 Hz) of the cell, measured with a bridge before the experiment, was 250 Ω, which compares favorably with the prebreakdown resistance shown in Figure 5. The channel resistance shown in the figure is plotted on a log scale which tends to straighten out the bend in the curve, as shown in Figure 4; hence, the toe on the curve is no longer obvious.

The voltage applied to the electrode was in the form of a pulse, and location of breakdown—leading edge, plateau, or falling side of the waveform — depended on the applied voltage and the gap distance. An attempt was made to achieve breakdown on the voltage plateau, which required a delay time to breakdown of less than 20 ns. The rather short delay time of less than 20 ns required that the peak voltage be increased with increasing gap distance, as shown in Figure 6

for distilled water. The voltage and gap distances shown give an average field ranging from 0.7×10^8 V/m to 1×10^8 V/m. Higher field strengths were required at the shortest distance; this is to be expected in normal breakdown phenomena. Jitter in the time was more severe at the longer gaps, possibly because of the reduced field applied. The maximum fields that could be applied were limited by flashover of the water test cell at the higher voltages.

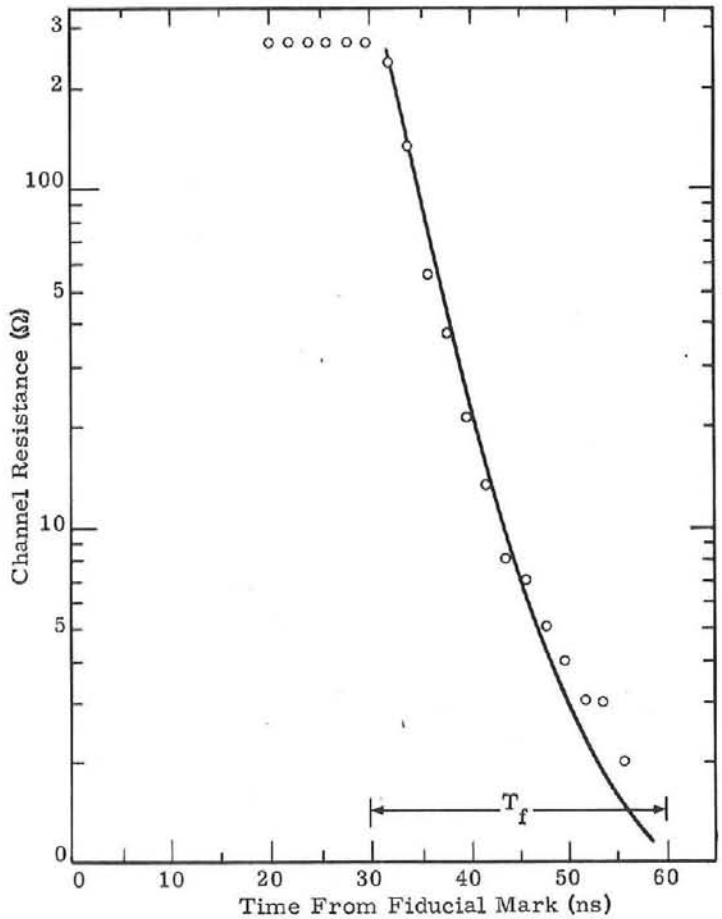

Figure 5. Resistance of Arc Channel in Formative Stage. Iron Electrodes 0.159 cm in Diameter Spaced 1.01 cm Apart

In obtaining the data shown in Figure 6 we determined that the formation of additional channels is controlled by the voltage applied and the delay time. Additional channels often formed in less than 20 ns when the average field exceeded 0.4×10^8 V/m. The voltage waveform does not clearly show the appearance of new channels, since it collapses after the first channel forms. Nevertheless, the current waveform usually showed steps that could be correlated in number to marks on the electrode and photographs of the spark. When the field was less than 0.4×10^8 V/m but greater than 0.1×10^8 V/m, additional channels formed in delay times greater than 20 ns. Additional channels, although not usually observed with pointed electrodes, were apparent when broad-area (diameter greater than gap distance) electrodes were used.

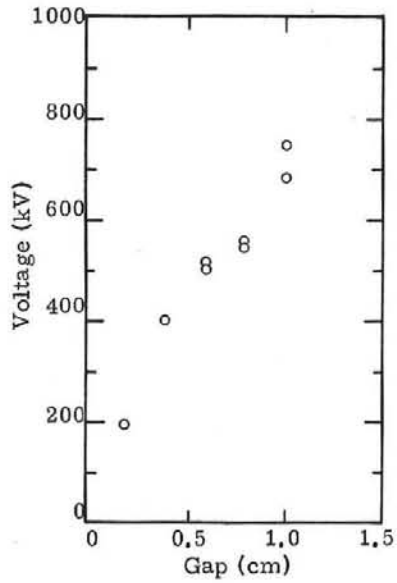

Figure 6. Voltage Required for Prompt Breakdown in Distilled Water (Delay Time Less Than 20 ns)

At the present time, spark drilling systems with lower voltage and higher inductance systems than those above are likely to be used. With the lower voltage, longer delay times will occur. If the delay time in dirty water is very long, stored energy will be lost by conduction in the water and pulse repetition rate may be limited. Hence, a simple capacitor discharge with a relatively high inductance system was used to obtain data. For example, the time delays for breakdown in tap water with 3-cm electrode spacing and voltages of 30-55 kV are shown in Figure 7. At 30 kV the jitter was large, ranging from 30 to 100 μs; below 30 kV the charge was usually lost without breakdown by conduction in the water; and above 30 kV jitter decreased, as did the time delay.

Voltages were measured close to the electrodes but, because of the jitter and uncertainty of breakdown voltage, the impedance during the formative time of the arc was not determined. Following breakdown, arc impedance was measured from the damped character of the oscillations. Arc impedance at various electrode spacings is shown in Figure 8. Since typical electrode spacings are expected to be less than 4 cm when a 20-cm hole is drilled, there is a problem of transferring energy from the electrical system to the arc (Figure 9). Arc impedances will be less than 100 mΩ, and generator output impedance is expected to be much higher. Figure 8 indicates that a long gap would help in giving higher arc impedance, and it would be easier to match the system impedance with load impedance.

Discussion of Results - The voltage and current waveforms similar to those shown in Figure 3, with an impedance curve of the type shown in Figure 4, can be used to estimate energy in the channel and energy density.

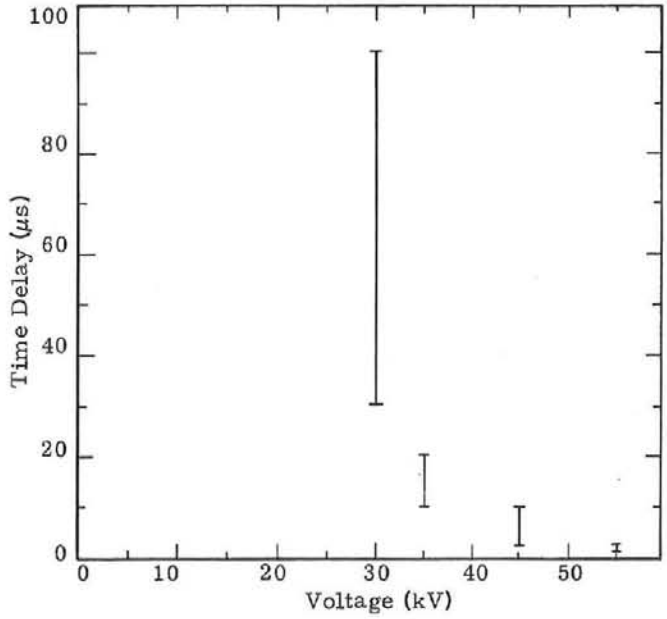

Figure 7. Delay Time to Breakdown With 3-cm Electrode Spacing

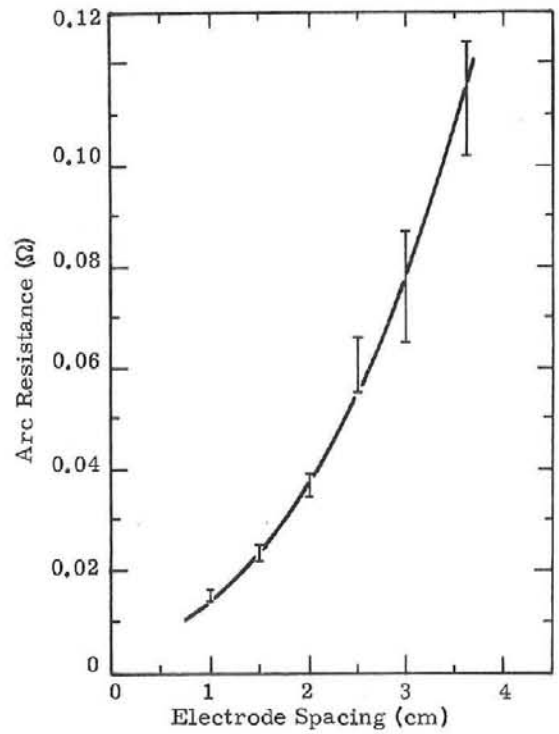

Figure 8. Electrical Resistance of an Arc in Tap Water

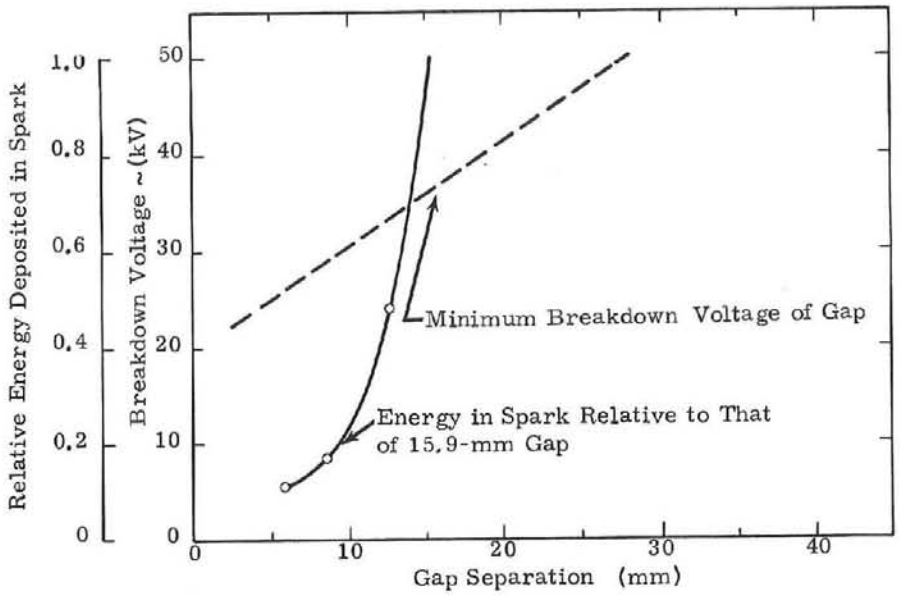

Figure 9. Energy and Breakdown Voltage vs Electrode Gap Spacing For a Typical Bit Configuration

Martin[1] estimates the particle density in the channel plasma as $2 \times 10^{27}\ m^{-3}$, the temperature as 30 000 K, and the plasma as 30% ionized.

According to our results the resistance of the channel R(t) is a strong function of the time, but after the fast impedance drop the resistance usually holds steady at a value of 2 Ω to 10 Ω for a period of time up to about 100 ns before declining further. This resistance at the toe of the curve increases with increasing gap distance; it is usually about 10 Ω for a gap of 1.5 cm and in the 2 Ω range for gaps near 1 cm. Here, we consider the case of a 1-cm gap and the channel for the toe of the curve at 1.5 Ω. The current in such a case is about 20 kA, as shown in Figure 3. The applied voltage then is about 30 kV, and the field is 2×10^6 V/m. The arc channel is probably in the early stage (during formation of the toe of the resistance curve), with pressures above atmospheric and the gas composed of hydrogen and oxygen. Estimates for the electron mobility may vary widely during this stage.[3] An estimation might be about 200 m/s per V/m. The velocity then is $v = (K_e)E = (2 \times 10^2)(2 \times 10^4) = 4 \times 10^4$ m/s. If the plasma is 30% ionized, as reported by Martin, the electron concentration is $\eta_e = 0.3 \times 10^{27}\ m^{-3}$ and the current density is

$$J = \eta_e eV = (0.3 \times 10^{27})(1.6 \times 10^{-19})(4 \times 10^4) = 2 \times 10^{12}\ A/m^2.$$

Here, the channel area would be the ratio of the current to the current density, or $10^{-7}\ m^2$, giving a channel radius of 1.7×10^{-4} m and a channel volume of $1.5 \times 10^{-9}\ m^3$. This predicts a larger channel radius than Martin's[4] estimates of 1.5×10^{-5} m based on other considerations. If one allows for the fact that the above calculation was for a time when channel impedance had dropped well below one-half the generator impedance and that Martin based his calculation on machine parameters and a solid dielectric, the channel radius of 1.7×10^{-4} m in water may be reasonable. The energy input in this phase can be estimated from the voltage and current waveforms at about 40 J, giving an energy density of $2.5 \times 10^{10}\ J/m^3$. Plumlee[3] has estimated a vaporization energy of $10^9\ J/m^3$ to initiate breakdown in n-hexane (estimate based on a very different approach) with a power input of $10^{18} J/m^3$-s. We obtain a power input of $2.5 \times 10^{17} J/m^3$-s for water, and for delayed breakdowns the phenomenon must be thermal in nature.

Very-high-speed photography is necessary for accurate measurements of channel expansion. Such equipment was not available to us because of heavy demand for its use.

The energy lost in delay time to breakdown (Figures 6 and 7) can be estimated for fluids by using an experimentally determined function of frequency (tan δ), given for pure low conductivity water in Reference 5. The time constant for a fluid, $\tau = RC = \left[2\pi(\text{freq})(\tan\delta)\right]^{-1}$, is independent of electrode geometry or energy sources. For the case of distilled water in the microsecond pulse region the time constant may be calculated as 4 μs. In other words, over 60% of the voltage on the electrodes will be lost in about 4 μs (if the electrodes are considered to be uncoupled from the source source in good high-resistivity water) without contributing to a spark pressure. Even more energy

is lost in high-conductivity liquid, such as drilling mud. The importance of prompt spark development after application of the voltage is clear if efficient energy transfer is desired.

Conclusions

A significant part of the work reported here is the resistance curve for water breakdown. This curve shows that the impedance between electrodes in water can change orders of magnitude in 2-3 ns as electrical breakdown occurs. This curve also led to the discovery of a toe on the curve where the resistance of the breakdown channel holds constant for a period of time in the 1-10Ω range before declining further. This toe has application in the design of a spark drill as well as of water switches. Energy transfer in the toe region is desirable in the first case and undesirable in the second. Optimum design in both cases must take the toe into account. Increasing gap length also increases the arc resistance, bringing about higher allowable output impedance of the electrical generator and thus simplifying design and lowering investment cost.

Others, in previous work, have noted an impulse effect in breakdown; that is, a dielectric can stand a higher voltage if the voltage risetime is decreased. In the present work, this effect is interpreted in terms of delay time to breakdown. Thus, the shorter the required delay time, the higher the required voltage. The consequences apply not only to the physics of the breakdown but to electrical generator design because the efficiency will be affected. Optimum efficiency is obtained with shortened delay time (conduction losses lowered), thereby again pointing up the desirability of using maximum practical voltage.

Electrical Energy Input to the Spark Channel

Summary

An expression has been developed for the energy deposited at the spark gap for early discharge times. It not only is shown to be more accurate than previously published expressions but indicates the direction a spark drill design should take. The energy is shown to be proportional to the applied voltage squared and inversly proportional to circuit impedance.

Discussion

The electrical energy input in the early stage of the breakdown in water is of practical importance because it is effective in developing the shock wave for the spark drill. Hence, in the design stage of a spark drill generator it is desirable to maximize the energy input, and a relationship for the energy input in terms of machine parameters is desirable as a design aid. The energy input relationship is derived here and compared to experimental results.

In the previous section of this report we have shown time-correlated voltage and current waveforms for the breakdown of water, together with curves for the time-dependent variation of the channel resistance in the first few tens of nanoseconds. Of significance here are major changes in those curves. It has been shown that four periods existed when the voltage was applied to the gap: a conduction and a charging current occurred for a delay period; a rapid increase in current started, together with a collapse in voltage and a decrease in the gap impedance (within 2-3 ns) by several orders of magnitude; the gap impedance held steady at 1-10 Ω for some tens of nanoseconds; and the gap impedance declined to the milliohm range.

The second stage (i.e., the rapid decrease in gap impedance) has been referred to as the resistive stage;[4] however, the designation seems more appropriate for the third stage, where the impedance holds constant. Here, we consider energy input to the second stage for comparison to previous work by others. Energy input to the third stage can be obtained in a similar manner.

Our oscillographic recordings of the voltage during the second stage in the breakdown of water show that the voltage collapse across the gap can be approximated to within 10% for oil and 10% - 50% for water by a linear relationship such as

$$V(t) = mt + V_o, \tag{1}$$

where V is the voltage, m is the slope (-V/s) of the voltage fall, t is the total time (s) required for the fall, V_o is the voltage at the start of the breakdown.

The waveform for the current rise in the electrical breakdown shows pronounced curvature. This curvature is controlled by the series inductance when the water resistivity drops suddenly so that

$$i(t) = \frac{V_o}{Z'}\left(1 + e^{\frac{-Z't}{L}}\right), \tag{2}$$

where L = henrys is the series inductance and Z' = ohms is the sum of the generator impedance (Z) and the arc resistance (R(t)). In the experimental arrangement used here the inductive reactance of the arc is small and will be neglected for Eq. (2). Although R(t) is not well known, our data show that it is a strongly decreasing exponential function of t. If Z is a few ohms, our data for this second stage show that R(t) will be in the neighborhood of Z for about 1/2 - 1/3 τ, where τ is the fall time. Because of this and because the power has a maximum at R(t) = Z, we will assume R(t) = Z. However, an exponential form for R(t) could be assumed with a large increase in the complexity of analysis and little increase in practical significance.

Then, to best approximation

$$i(t) = \frac{V_o}{2Z}\left(1 - e^{\frac{-2Zt}{L}}\right). \tag{3}$$

The energy into the resistive phase of the breakdown is

$$E(t) = \int_o^{\tau} v(t)\, i(t)\, dt \tag{4}$$

or

$$E(t) = \frac{V_o}{2Z}\int_o^{\tau} (mt + V_o)\left(1 - e^{\frac{-2Zt}{L}}\right) dt \tag{5}$$

and

$$E(t) = \frac{V_o}{2Z}\left[\frac{mt^2}{2} + \frac{mLte^{\frac{-2Zt}{L}}}{2Z} + \frac{mL^2e^{\frac{-2Zt}{L}}}{4Z^2} + V_o t + \frac{V_oLe^{\frac{-2Zt}{L}}}{2Z}\right]_o^{\tau}. \tag{6}$$

The second and fifth terms are equal but of opposite sign at $t = \tau$, since $m\tau \approx -V_o$, giving

$$E_{\tau} = \frac{V_o}{2Z}\left[\frac{m\tau^2}{2} + \frac{mL^2e^{\frac{-2Z\tau}{L}}}{4Z^2} + V_o\,\tau - \frac{mL^2}{4Z^2} - \frac{V_oL}{2Z}\right]. \tag{7}$$

The first and third terms are of opposite sign and may be added. Hence,

$$E_{\tau} = \frac{V_o^2\,\tau}{4Z} + \frac{V_omL^2e^{\frac{-2Z\tau}{L}}}{8Z^3} - \frac{V_omL^2}{8Z^3} - \frac{V_o^2L}{4Z^2}. \tag{8}$$

Observation of our oscillographic recordings of the voltage and current waveforms shows that a small amount of prompt energy is delivered in a time less than τ by the locally stored charge in the test cell and electrodes. Hence, a small-valued term should be added:

$$E\,(\text{cell}) = 1/2\, CV_o^2\,,$$

where C is the tube and electrode capacitance.

The final relationship for $\tau > 0$ is

$$E = \frac{V_o^2 \tau}{4Z} + \frac{V_o m L^2 e^{\frac{-2Z\tau}{L}}}{8Z^3} - \frac{V_o m L^2}{8Z^3} - \frac{V_o^2 L}{4Z^2} + 1/2\, CV_o^2 . \tag{9}$$

Using this relationship in a typical experiment where C, L, and τ are small, V_o is large, and Z is 10Ω or less, our calculations show that the first term tends to dominate the expression because the third and fourth terms and the second and fifth terms nearly cancel. It is interesting to note that the first term is identical to the J. C. Martin formula

$$E = \left(\frac{V^2}{4Z}\right) \tau_r , \tag{10}$$

except that our τ is the measured fall time and τ_r is a calculated time for the resistive phase (second stage). Martin derived his relationship for the energy in the resistive phase as follows:

$$E = I^2 Rt$$

and

$$I = \frac{V}{Z+R} .$$

Let

$$R = Z ;$$

then

$$I^2 = \left(\frac{V}{2Z}\right)^2$$

and

$$E = \left(\frac{V}{2Z}\right)^2 Zt$$

$$= \frac{V^2 \tau_r}{4Z} ,$$

where

$$\tau_r = \frac{5}{Z^{1/3} F^{4/3}} \text{ ns for solids and liquids.}$$

The constant, 5, in the numerator was determined experimentally by Martin.

O'Rourke[6] has also attempted a derivation of the Martin relationship. O'Rourke found that

$$E(t^*) \cong K \frac{V_o^2 t^*}{4Z} \quad , \tag{11}$$

where K is of the order of unity (K = 0.5),

$$t^* = k \left(\frac{\ell \rho_o}{E^4 Z} \right)^{1/3} , \tag{12}$$

E is in MV cm^{-1}, Z is in ohms, ℓ in centimeters, ρ_o is in g cm^{-3}, and k is arbitrarily defined as

$$k = 6 \frac{\rho_o^{1/6}}{\ell^{1/3}} \tag{13}$$

to ensure O'Rourke's t* being equivalent to the Martin τ_r.

We have not yet tested relations (9) and (10) for a variety of experiments. Experiment No. 676 was chosen at random to see how the numbers worked out. This experiment used 0.0016-m-diameter rod electrodes, spaced at 0.015-m increments, in distilled water of $\rho = 2 \times 10^8$ ohms/m. In this example, $L = 80 \times 10^{-9}$ H, $C = 50 \times 10^{-12}$ F, $Z = 8\,\Omega$, $\tau = 5.5 \times 10^{-9}$ s, $m = 3.8 \times 10^{13}$ V/s, $V_o = -2.1 \times 10^5$ V, $E_{calc} = 7.58 - 4.13 + 12.53 - 13.78 + 1.1 = 3.3$ joules, and $E_{meas} = 4.6$ joules (total). From the Martin formula $\tau_r = 35.7$ ns and $E_{calc} = 49$ joules.

Of greater importance at the present time is the value of the relationship for a design guide. The importance of the applied voltage and the machine output impedance is clear and, again, the need for high-voltage and low-output impedance is emphasized if maximum energy input into the second stage is desired. Choice of the value for Z would also be influenced by knowledge of the impedance during the third stage (toe of the resistance curve) for water breakdown. Considerably more energy (perhaps a factor of 10) could be put into the channel in this time interval.

Spark-Generated Environment - Pressure Measurement

One of the more important parameters in the spark discharge study is the magnitude of shock waves produced by the arc. A complete pressure/time history of the shock can be used to determine the pressure, impulse, and energy available for fracturing rock. Before this study, only approximate peak pressures were available in the near vicinity of the arc, and these were obtained

from photographs of the emitted shock wave. A lithium-niobate piezoelectric pressure transducer has been developed in this program to allow pressure history measurements at a point near the arc. The data from this gage, combined with photographic streak records, yield a valuable pressure record.

Development of the transducer has continued during this report period. It has been determined that the electric field created by the arc can cause dimensional change of the transducer and consequently generate a shock field of its own. Further investigations of the transducer are continuing to determine the minimum distance from the arc where acceptable data can be obtained.

In addition to the initial blast wave pressure near the arc in the fluid, the pressure wave transmitted through the adjacent rock must be measured. A transducer that can be embedded in the rock has been designed and tests are beginning. This transducer will also be used in the measurement of the pressure created by the collapse of the arc-generated bubble (see Effect of Fluid Jet on Spark Drilling Phenomena in Chapter 5).

This transducer is constructed in the shape of a disk. It can contain from one to seven lithium-niobate crystals, each acting as an independent transducer. The transucer is constructed in this manner to eliminate shear loading effects on the transducer in the embedded mode and to provide a stationary surface in the cavitation experiment. Analysis of the output of this transducer will be difficult because of the influence of the large disk on the pressure field. The problem of distortion is always present, since a transducer has finite size.

Investigation of the shock waves created by the arc discharge has yielded some interesting results. When the energy is deposited over several microseconds, the shock pressure does not attenuate rapidly as it radiates from the arc channel. When the energy is deposited in nanoseconds, the shock pressure attenuates rapidly, as expected. Also as expected, the peak pressure is much lower when the energy is injected over a longer time period. Peak pressures at the edge of the channel, as determined from streak records, appear to be in the neighborhood of 4 GPa for the dicharges generated by the pulse generator (described in Chapter 2) where most of the energy is injected in less than 40 ns. This compares with peak pressures of less than 1 GPa when a somewhat larger amount of energy is inputted in several microseconds.

Energy Density of the Channel

Channel energy-density values are necessary for the predictions of stresses in the drilling fluid as the result of an electrical discharge. Maximum values of energy density[7] have ranged from 7000 J/g* to 10 000 J/g . In Chapter 2 of the present report calculations indicated that the value could be as high as 25 000 J/g.

One method of determining the energy density is to measure the electrical energy in the spark and record the volume of the channel as a function of time by using a high-speed camera. The speed of the camera must be in the nanosecond range. Sandia Laboratories has two of these but, because of the heavy demand for them, they have not become available for this application.

An estimate of the energy density can be obtained if the peak pressure generated by the arc can be measured. A peak pressure of 4 GPa has been obtained from streak camera records. Through the Grüneisen relationship this pressure represents 4000-J/g energy density. It is recognized that the streak records show only a change in density and that the Grüneisen relationship applies only to instantaneous energy deposition. The camera record, therefore, would indicate only half of the instantaneous value, so the peak energy density would be 8000 J/g.

Because of the great range of values, both reported in the literature and calculated, it is clear that more effort is needed for determining the value more precisely.

---

*Calculated from data in Reference 1.

Chapter 3

DYNAMICS OF A SPARK-GENERATED BUBBLE IN A HIGH-PRESSURE FLUID

Summary

Extensions of studies of arc discharge in tap water provided bubble-dynamic and shock-wave generation data as a function of hydrostatic pressure to 69 MPa (10 000 psi). Preliminary analysis of data indicates that the shock-wave pressure generated by the creation and expansion of a 1-mm-long arc in water remains essentially constant (~ 2 kbar) with hydrostatic pressure. As energy to the arc is increased (provided by increase in stored capacitance) the bubble size increases, but shock-wave pressure appears to remain essentially the same since it is mainly a function of applied voltage. Maximum bubble size at 69 MPa was approximately 9 mm in diameter, with an arc energy of approximately 150 joules.

Discussion

Modification of the bubble dynamics pressure vessel to extend its capability to 69 MPa has been completed. Additional modifications were required for eliminating electrical surface breakdown problems in the electrode assembly. Further, redesign of the electrode assembly will be required in order to extend the usefulness of the equipment to higher operating voltages and energies.

This reporting period has provided data wherein the hydrostatic pressure and arc energy are varied and the arc length is held constant. To vary the arc energy, capacitance was increased and the voltage was held constant. It would be more desirable to vary the voltage and hold the capacitance constant in order to provide greater variance in di/dt (where $di/dt = V/L$). Upper voltage limitations, about 25 kV, on the electrode assembly prevented the use of this option. As a consequence, for this series of experiments, the variation of di/dt was small. Data obtained consisted of simultaneous high-speed streak and framing camera coverage and load-circuit current waveforms. From these data, the bubble dynamics, shock-wave velocity, arc resistance, and arc energy were estimated. Preliminary statements concerning the experimental results can be summarized as follows:

1. The electrical characteristics of the arc are not affected by hydrostatic pressure to 69 MPa; the current waveforms remain essentially constant. With a di/dt of from $2\text{-}2.5 \times 10^{10}$ amp/s, and of an oscillatory nature, the arc resistance is estimated to be approximately 0.04Ω for late times. Peak currents ranged from 25 to 45 kA.

2. The shock wave generated by the arc discharge averaged approximately 0.2 GPa (2 kbar) as calculated from the equations of state of water and the measured shock-wave velocity at 17 mm from the arc.

   Since only two-dimensional camera coverage was obtained, it was assumed that the arc channel occurred parallel to the lens. Deviations from this introduce error in interpretation of the data. An attempt was made to measure the channel growth as a means of obtaining particle velocity. Because of the high streak-record velocities, the shallowness of the arc channel was such as to introduce large errors to the reading of the film record. Other hazards, such as variations in the edge sharpness in viewing a pulsating growing channel perpendicular to its axis, introduced additional errors. In general, shock-wave pressure was found to be 20% to 30% greater by this method.

3. Under hydrostatic pressure above 6.9 MPa (lower limit of pressure for the series), the void ("bubble") created by the arc discharge does not behave in the classical ambient pressure manner. The diameter of the void, as would be expected, diminishes with increased hydrostatic pressure until, at the lower arc energies, the void appears to coincide with the diameter of the arc channel. As the arc energy is increased, some slight increase in diameter is seen at the 69-MPa condition. In no case did the void attain a diameter greater than ~9 mm at this pressure. Therefore, we detected no evidence of jetting during the test series while viewing the 160-μs test exposure periods. Although it is recognized that shock waves reflecting from the chamber walls were interfering with the bubble growth, the chamber did represent a realistic bore hole.

Chapter 4

HIGH-ENERGY SPARK DRILL SYSTEMS

Summary

A laboratory spark drill system has been designed and is being fabricated to allow the experimental determination of feasible drilling rates in various rock types. Its output characteristics are as follows: 1500 J of stored energy per pulse, a current rise rate of 10^{11} amp/s, a pulse rate of 10/s, and a circuit inductance of less than 1 μH. The quality of the spark is such that extrapolations of drilling rates can be made to the desired power level (112 kW). Fabrication is approximately 50% complete, and we plan to have the system operating by April 1, 1976.

Desired Design Characteristics

A laboratory spark drill system is required for support of the program research phase, with pulse characteristics and repetition rates sufficiently high to determine potential drilling rates in various rocks. Our present laboratory system has not fulfilled these requirements. The experiments to obtain the electrical characteristics of a fluid during a spark discharge confirmed that high discharge voltage, together with low system impedance, is required to give acceptable spark efficiency. Experiments conducted on our present laboratory spark drill indicated that the system efficiency went up almost exponentially with increasing gap spacing (Figure 9). Early in the report it was shown that the voltage magnitudes required for prompt discharges increased as the gap spacing increased. A minimum potential for prompt ionic-type discharge is reported[8] to be 3.6 kV/mm. A design compromise is then required between gap spacing and the practical limit of voltage allowed.

Calculations performed to determine the energy per pulse desired indicated that 380 J's were required to fracture Berea sandstone when the following parameters were assumed: a 10-mm spark standoff from the rock surface, spark duration of 1/2 μs or less, and 10 000-J/g peak channel energy density. The efficiency of energy transfer from electrical to shock wave is not known, but an estimate of 30% was made despite the fact that some reports have indicated a much lower efficiency. Our assumption results in a system which must produce 1000 J per spark in the fluid. From the analyses of the spark-generated bubble collapse time, with five oscillations to quiescence allowed, the system could have a repetition rate of 20 pulses per second per electrode. To eliminate interference of one electrode pair with another, we decided to design the system with a total of 10 pulses per second.

In addition to consideration of the spark drill bit in the design of the pulse generator system and consideration of the electrode gap spacing, the number of electrode pairs must be addressed. In an effort to design a low inductance system and to minimize high-voltage stressing of the bit insulator material, it was decided to design a four-electrode-pair bit.

The above considerations constitute the design characteristics of the new laboratory drill system: 1000 J of energy per spark; minimum inductance, 10 pulses per second; and a four-electrode-pair, 24.8-cm-diameter bit. The system has an average power of 10 kW (13.5 hp). Although this power is quite a bit lower than the 112 kW (150 hp) believed to be desired in future spark drill systems, it would give results that could be extrapolated to the higher power.

Design Approach

Feasibility of spark-drilling various rock types can be determined by the results of drilling experiments. Such experiments were attempted at an early time and at minimum expense by using available laboratory equipment and by conducting laboratory drilling experiments. This required the average power to be less than originally desired, with the quality of the spark degraded to a point where meaningful drilling rate data could not be obtained.

The new system has been designed by using available components and power supplies. A simplified circuit diagram of the pulse system is shown in Figure 10. In this system the repetitive pulse output for each of the four electrode pairs of the bit is provided by a separate 0.8-μF capacitor, which is successively charged and discharged to provide an output of approximately 65 kV across the electrode pairs of the bit. Loop inductance of each discharge circuit will be as low as practical (600 nH or less) so that peak currents greater than 50 kA can be achieved. High-energy, voltage-sensitive spark gaps will be used to close the output circuit. The stored energy at the time of each discharge will be about 1500 joules. These output capacitors will be pulse charged from a three-stage Marx generator used to multiply charging voltage from $\sim$25 to $\sim$75 kV. The output of the Marx circuit will be triggered and sequentially commutated to the four output capacitors by a motor-driven switch.

The four output circuits, shown in Figure 11, are enclosed in a cart assembly which can be rolled onto a rack which allows the cart to surround the spark bit stem and be supported directly above the experimental tank. This output pulse-forming assembly will have a volume around 0.7 to 1.0 m^3 and will weigh about 450 kg.

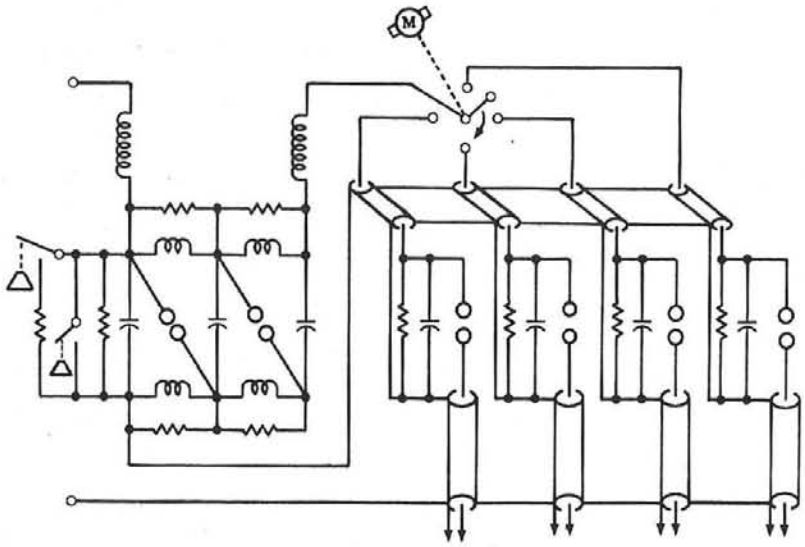

Figure 10. Simplified Circuit Diagram of Pulse Generator

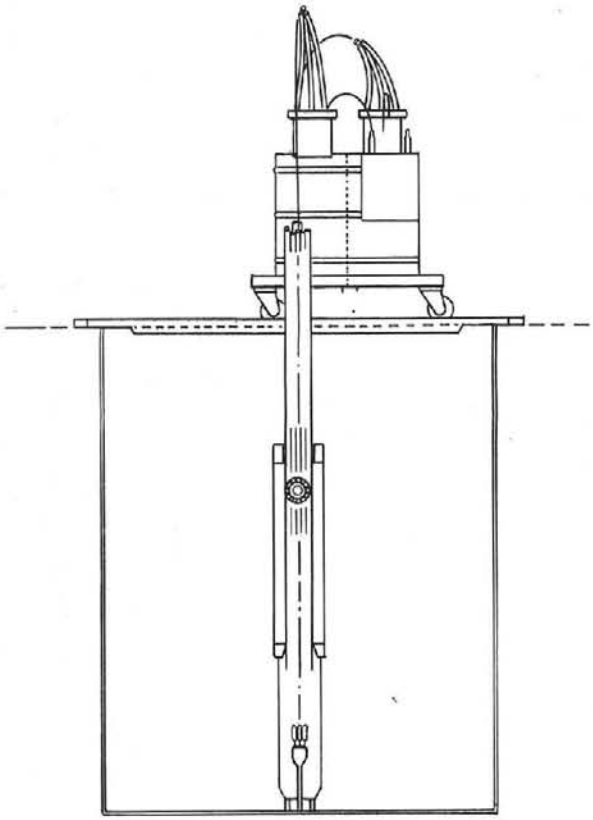

Figure 11. Pulse Generator Assembly

According to the circuit diagram of Figure 11, the input charging capacitance of the voltage-multiplying Marx circuit will be about 6.0 μF as its three 2.0-μF capacitors are charged in parallel. Each time the pulse-charging rotary switch swings to a new output circuit, it will connect the Marx circuit to an output capacitor. The two remaining spark gaps will be self-triggered and, as the three capacitors then become connected in series, the Marx will begin pulse-charging one of the four spark output circuits through the pulse-charging inductor. Output capacitance of the Marx will be about 0.66 μF as its three capacitors are discharged in series. The pulse inductor, wound with an inductance of greater than 70 μH, acts to lower the ringing frequency of the resonant circuit created by sudden connection of the Marx to the output capacitor. It also aids in transferring more of the Marx energy to the output capacitor and broadens the available peak of the output capacitor voltage waveform. These actions make triggering of the output switching gap and the bit electrodes less critical with respect to charge timing.

The pulse inductor is packaged in the same oil tank as the Marx capacitors and their charging-circuit isolation coils. The overall volume of the oil-filled Marx system is about 1.0 m^3 and it may weigh nearly 1000 kg.

The Marx will be resonant charged through a 180-H charging reactor to limit and control the input charging current from a 50-kW DC power supply. The separate oil-immersed reactor, purchased from a commercial supplier, will also weigh in the vicinity of 1000-1500 kg.

The rotary switch is actually composed of four pairs of stationary electrodes, each switched by a moving 0.64-kg trigger electrode inserted through the wall of a closed spinning drum enclosing the high-voltage-electrode portion of each pair. The switch drum is driven by a three-phase 249W (1/3 hp) gearmotor at 150 rpm to provide 10 pulses per second (2-1/2 pulses per second at each of the four outputs). An elevation view and a top view of the switch are shown in Figures 12 and 13, respectively. Input and output connections of the switch are immersed in oil. The spinning drum is made of high-temperature, high-quality insulation materials and weighs around 6.8 kg. Air flushing of the switch provides cooling.

The bit shown in Figure 14 will be used in the initial drilling experiments. A controlled-field-gradient bit is being designed and will be fabricated.

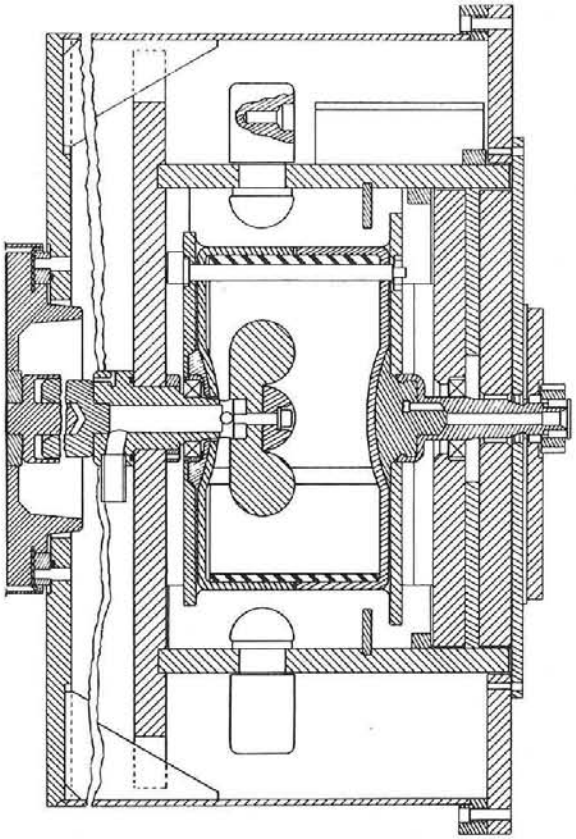

Figure 12. Rotary Switch - Side View

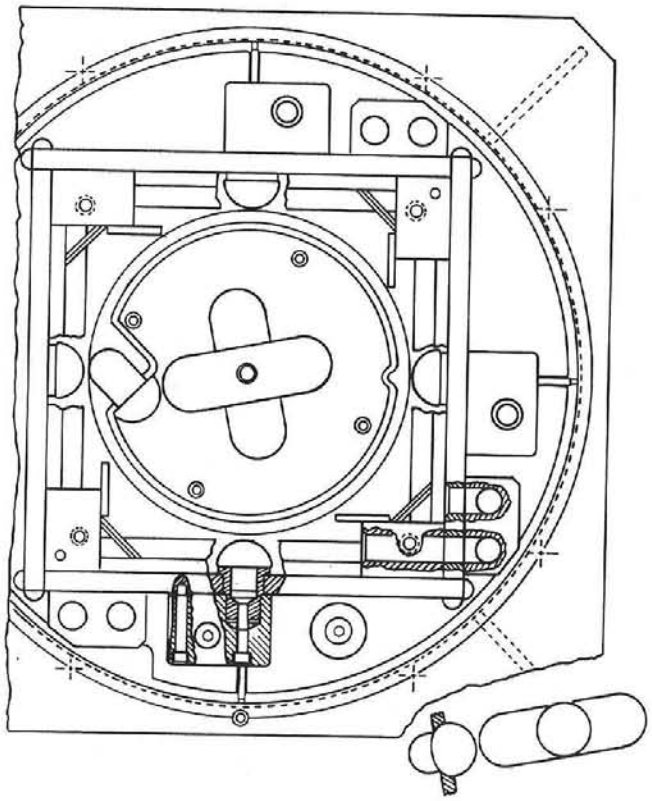

Figure 13. Rotary Switch - Top View

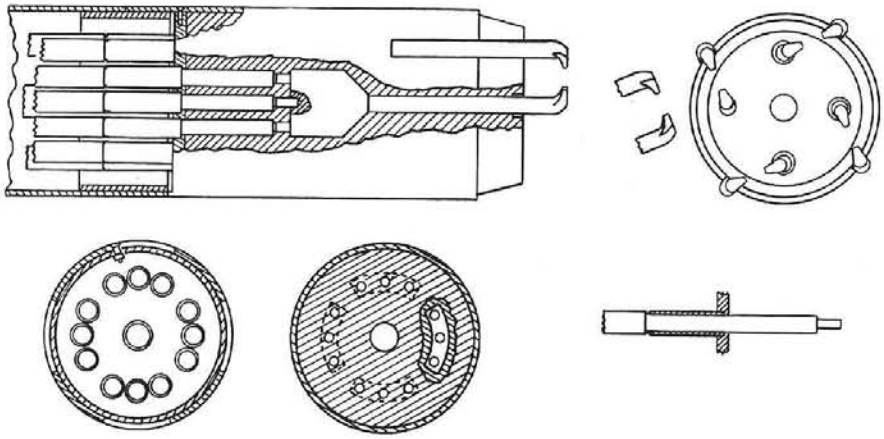

Figure 14. Exposed Electrode Bit

Design and Fabrication Status*

We have set a goal to have the system in operation by April 1, 1976. Although much work must be done between now and then, the goal is believed to be realistic.

The following gives fabrication status of individual components:

Marx generator: Under construction - 50% complete

Rotary switch: Under construction - 90% complete

Charging reactor: Outside purchase - delivery scheduled for February

50-kW DC supply: Outside purchase - on hand - needs to be checked out

Spark gaps; On hand - breakdown adjustment experiment in process

Grease rack: In fabrication - completion scheduled for February 1

Pulse generator: In fabrication - parts due February 1

Exposed electrode bit: In fabrication - piece parts due January 19

The controlled-field-gradient bit, which is in the design stage, should be completed by February 1 and fabricated by April 1, 1976.

*Editors Note: At the time that this report was written it was anticipated that the FY76 funding level for the spark drill research program would be near the requested level, and milestone schedules were based on this assumption. Since the higher funding levels have not been approved by ERDA/Division of Geothermal Energy, key dates in this report should be slipped approximately 6 months.

Chapter 5

SPARK DRILLING EXPERIMENTS

Summary

Spark drilling experiments showed that the mode of rock failure changed from tangential cracks near the surface to radial cracks at greater drilling depth. Subsequent petrographic analyses indicated that the fractures were still extensional in nature. Additional experiments were conducted to determine when the rock fractured as a result of the spark, to evaluate a new bit design, and to study the effect of interrupting a mud jet with a spark. The information obtained will aid in future design considerations.

Ejecta Experiments

Experiments were made to observe the time that ejecta takes place on soft-rock-like material in relation to growth and collapse of the bubble. All experiments were made at ambient pressures using needle gaps placed approximately 5 mm from fire brick. High-speed photographic coverage was made from 3000 to 130 000 frames per second. A cone-shaped cavity was created by a single-pulse discharge. Some small percentage of the material was observed to be removed when the shock wave impacted the material. The expanding shock wave and subsequent bubble hold most of the material in compression until the surface is relieved, at which time the balance of the material is ejected. This information, however, was not sufficient to indicate when or how the fracturing of the rock was accomplished.

Indiana Limestone and Berea Sandstone

Drilling experiments in our laboratory conducted on limestone and on sandstone utilized our pulse generator system and four-electrode, 140-mm O.D. bit (Figures 15 and 16). The rocks were then sawed into laboratory-manageable slabs and sent to Texas A&M University for petrographic analysis.[8] Of these two types of rocks, the sandstone was easier to drill.

An attempt was made to spark-drill granodiorite with the same drill system; however, for all practical purposes, the system failed to drill the rock. The voltage on the system was limited to approximately 40 kV and, because of the 4-μH system inductance, the current rise was too small to create high-strength shocks. When a low-inductance circuit was designed and connected to the one-electrode controlled-field-gradient bit, the granodiorite was fractured in only a few sparks. The rock was not considered to be drilled, however, as the bit was too large to follow the hole that it made.

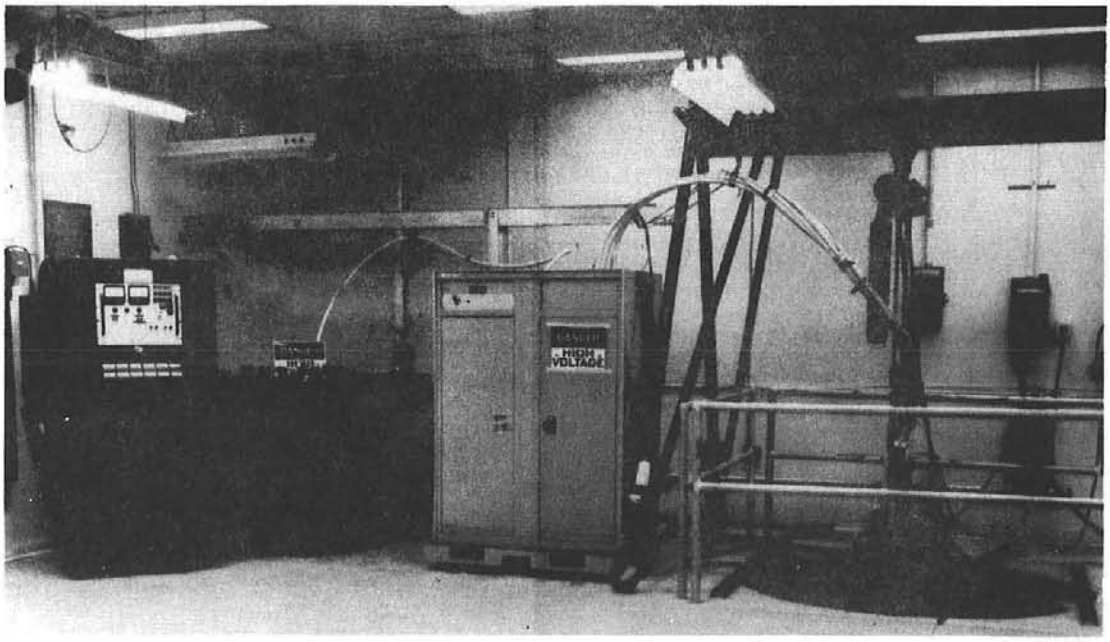

Figure 15. Present Laboratory Drill System

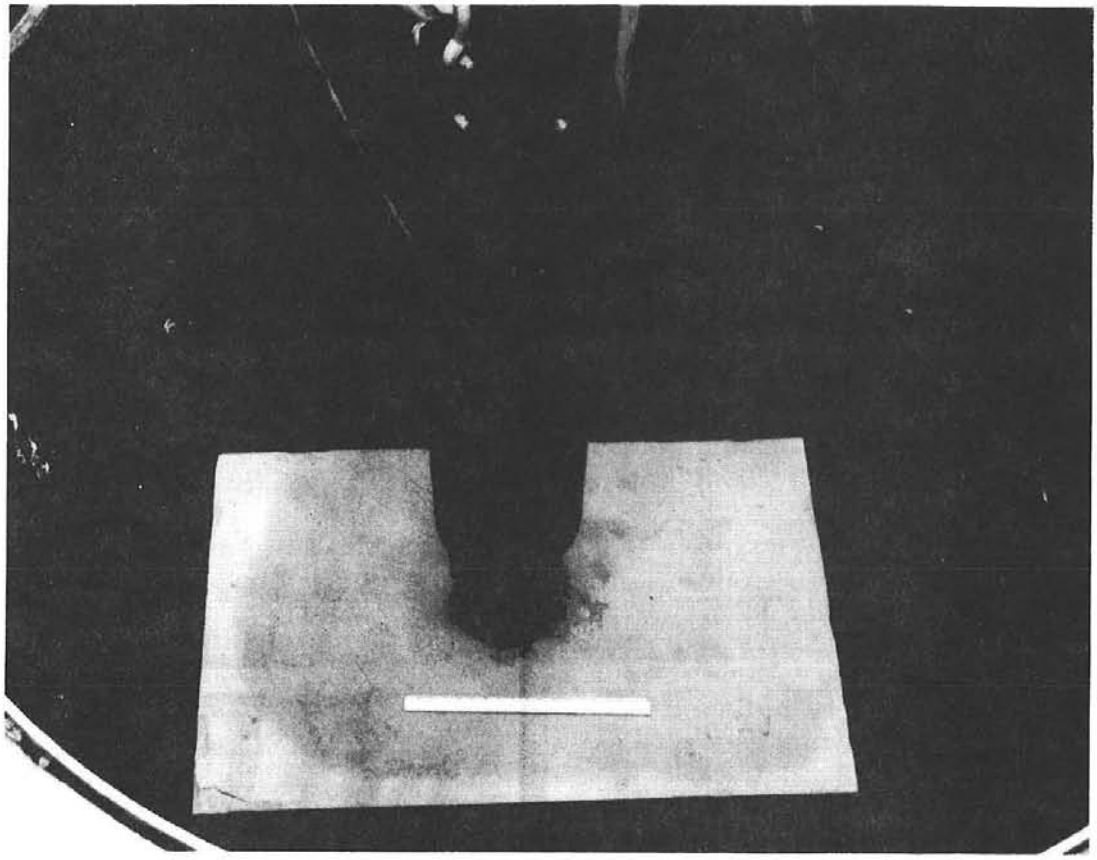

Figure 16. Present Laboratory Drill Bit
and Experiment Chamber

Petrographic analyses indicated occurrence of three types of fracture: spall, cone, and high-angle fractures (Figure 17). Neither the spall nor cone fractures, fundmentally tensile, showed shear offset. Their paths were controlled only locally by grain boundaries, cleavages, or preexisting microfractures; i.e., in the main they followed expected stress trajectories. The spall fractures were oriented essentially parallel to the bottom of the drilled hole. They probably originated from tensile stresses parallel to the hole axis that developed upon the relaxation of the rock after passage of the original compressional wave and upon collapse of the "bubble" in the drilling mud. It is possible, however, that they could have been caused by point loading (developed in the Hertz theory). Cone fractures occurred along the surface of downward-opening, nested cones the axes of which were congruent with the hole axis. These fractures, which were inclined at about 60° from the top surface of the drilled block and dipped away from the lower end of the hole axis in all radial directions, were probably tensile fractures formed along the trajectories of the principal compressive stress resulting from the compressional shock wave. The third type of fracture was developed at 0° - 30° from the hole axis. Since these fractures often dipped toward the lower end of the hole axis, they were not cone fractures. Some showed shear offset and gouge, and others exhibited no shear displacement. Some were thought to be shear and others to be tensile failures. The cone fractures were the predominant mode of fracture in the drilling experiment.

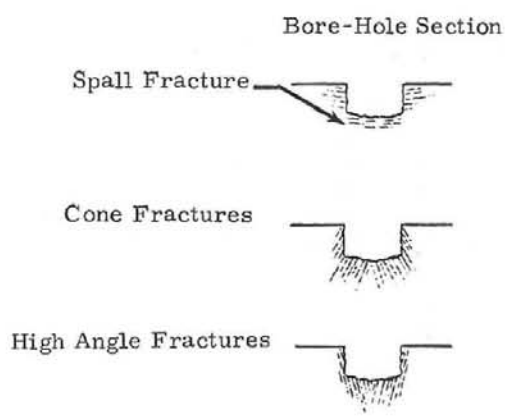

Figure 17. Types of Rock Fracture

Microscopically, there was little if any twin gliding in the calcite of the limestone adjacent to macrofractures. The fracture propagated along grain boundaries and through grains in about equal proportions. There was no evidence of shear displacement, only separation normal to the fracture walls. Microscopic fractures paralleled macroscopic ones. Thin sections of Berea sandstone have not yet been studied.

In summary, the results are essentially the same as those reported for shallow drilling. The main exception is that the fractures changed from tangential (spall) fractures to concentric radial ones with depth. Why this occurred is not fully understood.

Effect of Fluid Jet on Spark Drilling Phenomena

In drilling it is necessary to circulate a fluid to remove the cuttings generated. Fluid flow velocities of 200 m/s at the bit are commonly used. Since this stream contains a considerable amount of kinetic energy, it is desirable to determine the effect of a liquid stream on an arc discharge.

Desirable effects include addition of particle and jet velocities to create higher blast (shock) wave pressures, interruption of the jet to create impact (water hammer) conditions, and enhancement of the cavitation bubble collapse. Possible undesirable effects include increased breakdown voltage, weakening of shock wave because of gas bubbles in the stream, and increased erosion of electrodes.

Preliminary experiments have been conducted to evaluate the experimental equipment. These tests indicate that there is addition of particle velocity to the jet velocity and that the jet is interrupted for low velocities (30 m/s). In higher velocity jet experiments (up to 175 m/s) the water contained dissolved air which precluded informative results. At elevated fluid pressures the dissolved air expands as it comes through the nozzle, enlarges the stream, and reduces arc resistance. Also, the small air bubbles cloud the water so that photographic coverage yields little information. A simple gas/liquid separator which has been built will be tested in the near future.

One of the more promising features of this technique is that the problem scales well at the high hydrostatic pressures present at the bottom of a bore hole. This scaling, although helpful in actual drilling conditions, makes the cavitation experiments difficult to model. The bubbles generated at atmospheric conditions expand to excessive size; therefore, the bubble life is long when compared to the time required for the jet to pass through the affected region. For experimental purposes at atmospheric pressure, special conditions must be created for using a jet to aid bubble collapse. The conditions are low jet velocities (30 m/s) and small bubbles (10 mm in diameter).

With the aid of a high-speed framing (200 000 frames/s) and streak camera and the multiple lithium-niobate transducer the following can be determined: effects on the pressures generated by the shock wave in a stream, impact of the interrupted jet, and cavitation bubble collapse. The system will also be used to determine the collapse pressure generated by a cavitation bubble without high-velocity flow.

Bit Experiments

A bit was designed in such a way that the gap spacing would be small, then enlarge as the arc progressed toward the rock to be drilled. The insulator of the one-electrode bit, shown in Figure 18, was alumina, and the metal parts were made from Kovar. The alumina was prepared so that the Kovar made a metallurgical bond to it. After approximately 50 discharges, the insulator failed and the bit stopped drilling. The generated stresses also swelled the end of the bit into a bell shape (Figure 19). It is apparent that the design is limited because of its insulator material.

The four-electrode bit described in the previous report was modified by forming recesses in the insulation around the anodes to eliminate insulator surface spark-over. The recesses, which replaced the spheres, have performed very well: operating for several thousand pulses without failure. This modification is shown in Figure 20.

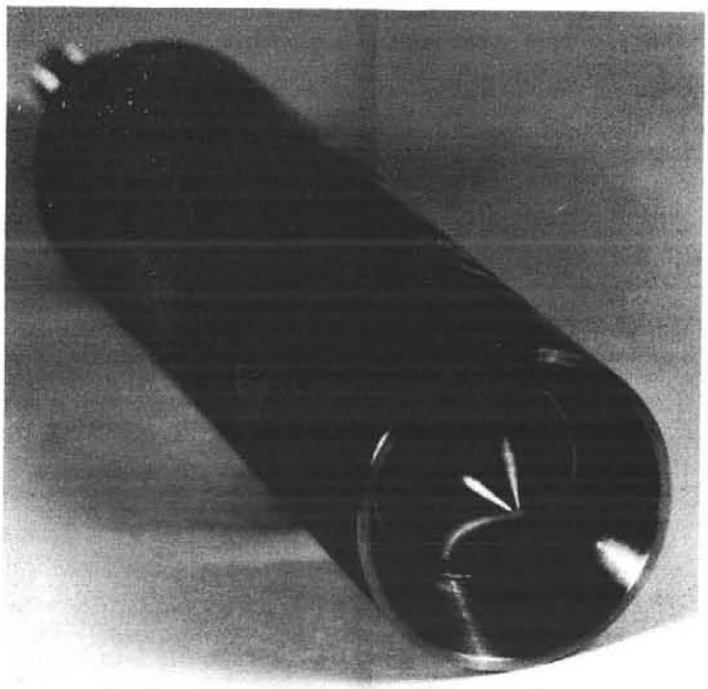

Figure 18. Conical Bit Design

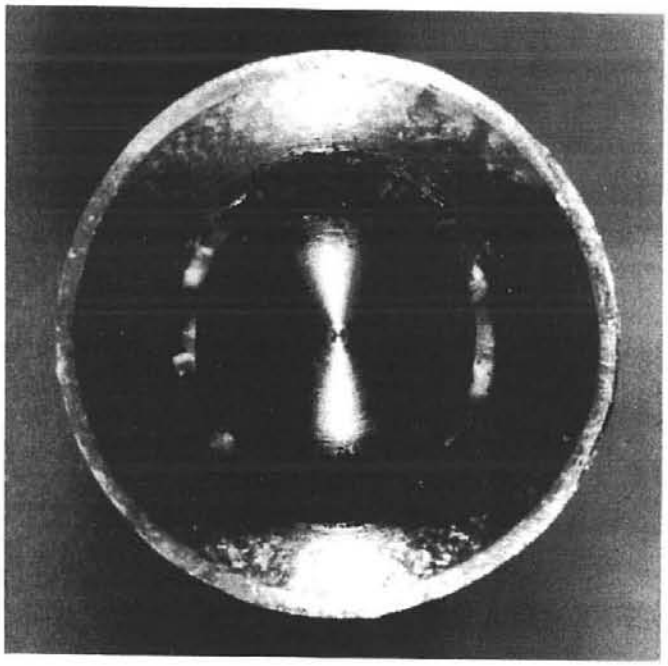

Figure 19. Conical Bit After Test

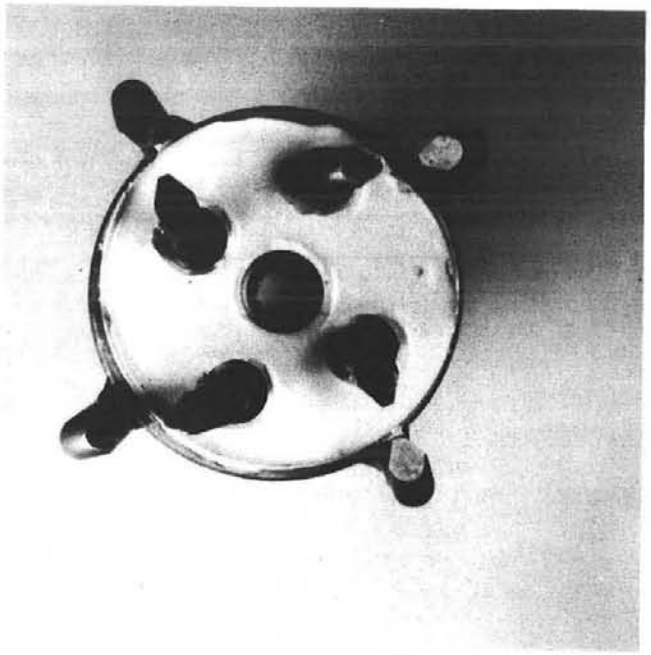

Figure 20. Exposed Electrode Bit

Chapter 6

ROCK-FRACTURE INVESTIGATIONS

Summary

Indiana limestone and Berea standstone subjected to a single-discharge spark drill environment have resulted in spark drill failure envelopes. Although most of our drilling has been done at energies below those indicated to cause failure in compression, the drilling is believed to be the result of tensile failures caused by multiple spark damage effects upon the rock. Actually, our drilling rates appear to follow those of a typical erosion process. The new laboratory drill system is expected to perform at or above the indicated failure energy and, therefore, above the threshold energy level of the erosion rate curve. The failure modes found during drilling experiments will be used to improve drill bit design.

Discussion

Failure envelopes have been generated for Indiana limestone and Berea sandstone by utilizing the scaling laws we generated for spark discharge in a fluid and the compressive strength properties of the rocks. These envelopes, shown in Figures 21 and 22, represent the upper limits of rock strength. It can be seen that the failure envelope consists of a large band of energies for a given standoff distance. The bottom of the band is derived for uniaxial stress conditions which could occur for near-static loading conditions. The top of the band, derived for uniaxial strain conditions, is representative of dynamic loading. Therefore, spark drilling energy levels for compressive failure would be closer to that for uniaxial strain.

Spark discharge experiments have resulted in very little or no visible damage in the limestone or sandstone from a single spark discharge. When a number of discharges have occurred, rock has been fractured and drilled. The experimental drilling results indicate that the drilling rate follows a typical erosion curve, as shown in Figure 8. Our experimental spark energies have so far been below the failure threshold level, where the drilling rate increases abruptly. This indicates that the failure mechanism in the rock is in some way related to time. One of the axes of Figure 23 is shown to be time, but just how it is related is unknown at present.

Only a few shear failures have been observed in our drilling experiments. This may be the result of rock being loaded in compression by the compressive shock wave and by the overburden pressure, which increases the shear strength of the rock. This characteristic is similar to the relationship shown in Figure 24. With the compression shock wave radiating outward in a spherical shape, there will be only shear stresses associated with compression and, from the shear strength/compressive strength relationship, the rock will be shear-resistant. This problem has been

analytically modeled by Sandia's Solid Dynamic Research Division. The solution, which is being programmed onto the computer so that a stress relationship within the rock can be predicted, will aid in bit design as the bit can be designed to have load discontinuities instead of the spherical radiating shock wave. The controlled-field-gradient drill bit design develops a load discontinuity around the periphery of the bit opening.

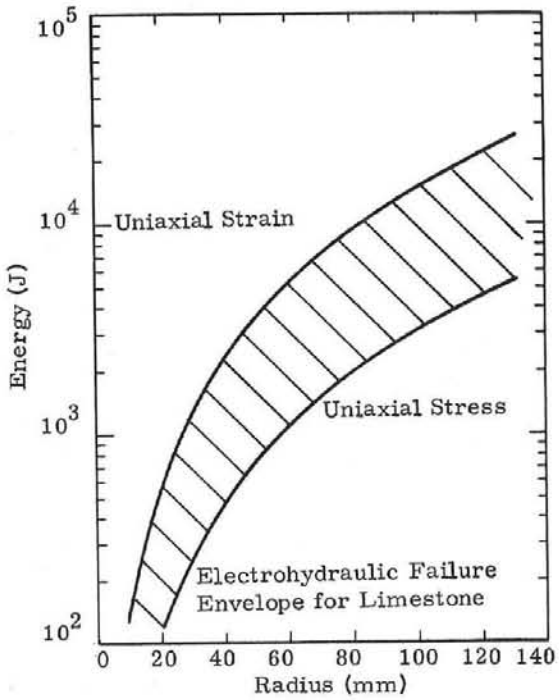

Figure 21. Failure Envelope for Indiana Limestone

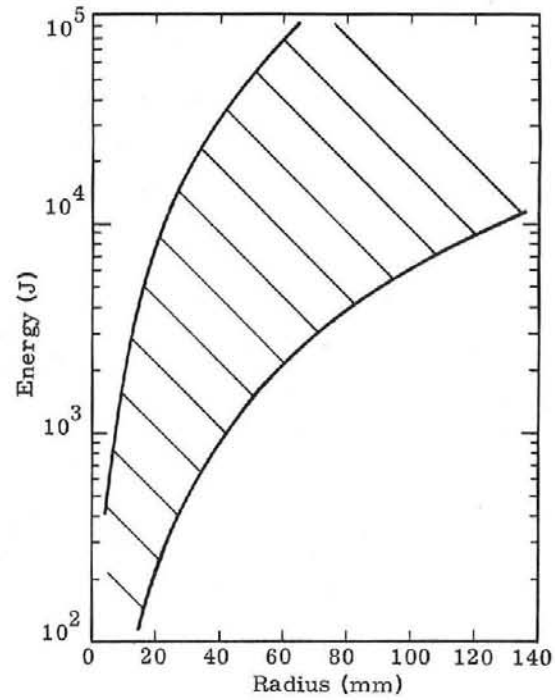

Figure 22. Failure Envelope for Berea Sandstone

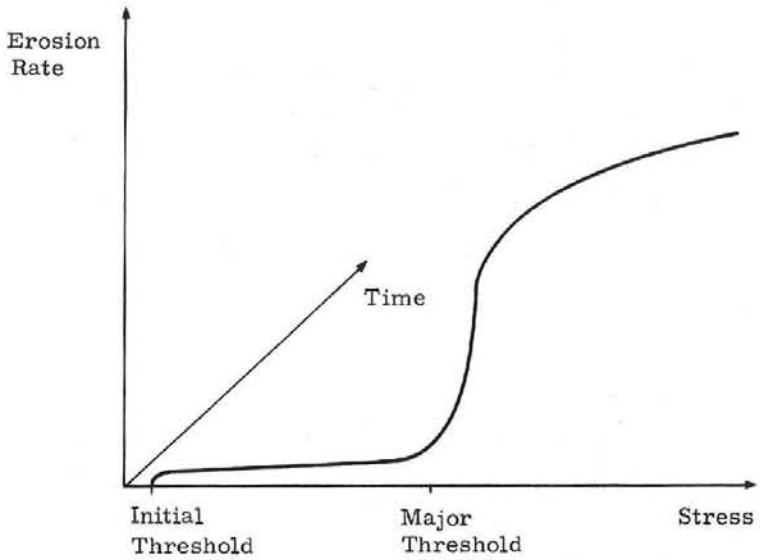

Figure 23. Typical Erosion Characteristics of Materials

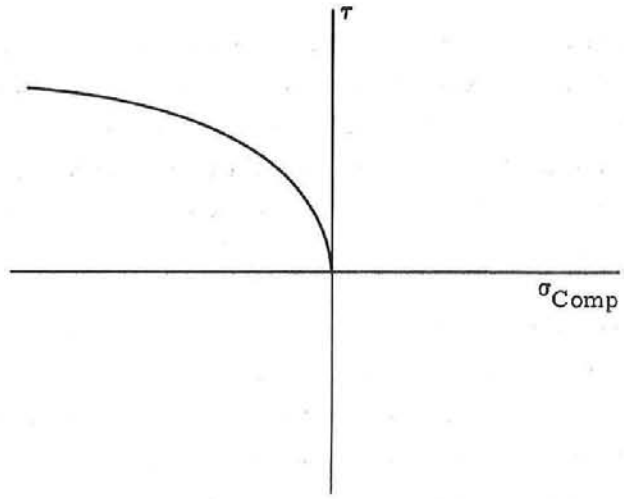

Figure 24. Typical Shear Strength vs Compression Stress

Two-dimensional hydrodynamic analysis has been done to determine the stress generated in the rock by a spark drill. The resulting stress in the rock has been desired at points remote from the bore-hole wall and near the wall. As our two-dimensional codes are for axisymmetric problems, this problem was analyzed by changing the bore-hole size as shown in Figure 25. The spark characteristics used were 1000-J total energy, 10 000-J/g energy density, 1/2-and 2-μs deposition time, and with a rock/spark standoff distance of 8.85 mm. The bore hole was at an overburden pressure of 6.9 MPa (1 ksi).

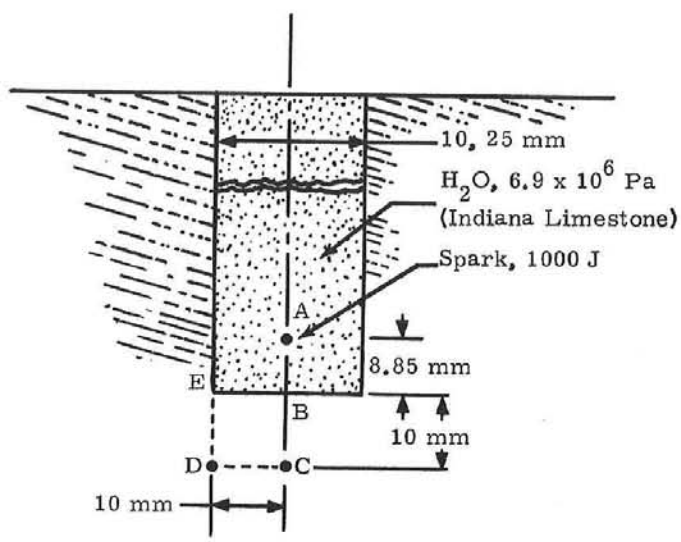

Figure 25. Diagram of Two-Dimensional Stress Problem

The stresses at positions marked A, B, C, D, and E were determined as a function of time. In comparing the results, the following conclusions were reached: (1) The peak compressive stress in the limestone was the same for both bore-hole sizes and (2) the magnitude of the stress and the stress history at points C and E were essentially identical for both 1/2- and 2-μs deposition time. These calculations are valuable because of the difficulties involved in making accurate in situ measurements with transducers.

This analysis and the shear strength consideration of the rock will aid in improving spark drill bit designs. These results indicate that bits which produce discontinuous shock waves are desirable and that the shock wave need not be in the periphery of the hole to obtain maximum stress within the rock. The magnitude of the calculated stress in rock will aid in determining the effect of the transducer body on the experimental stress measurements.

Chapter 7

MULTIPURPOSE ENVIRONMENTAL TEST SYSTEM

Summary

Engineering research and design efforts have been in progress since September 1974 to develop a multipurpose environmental test chamber (Figure 26) with supporting facilities to simulate deep-hole environments that are encountered in drilling and/or well testing. This vessel will be used for environmental testing of the various drill bits and logging sondes.

The severe design requirements represent conditions that will be encountered in 9000- to 12 000-m-deep oil exploration wells or 5000- to 6000-m-deep geothermal wells are as follows:

1. A maximum operating pressure of 206 MPa at 343°C or 138 MPa at 399°C.
2. Fluid circulation of 568 litres per minute.
3. Provision to dissipate heat from 330-kW input while maintaining a temperature of 232°C.
4. Internal vessel cavity of 0.305-m diameter and 3-m length.
5. One instrumentation feedthrough which has 10 conductor pins.

The complete system will consist of a pressure vessel, piping, line coolers, line heaters, circulation pump, pressurization pump, and vessel mounting structure. Design improvements incorporated recently on the vessel are as follows:

1. A hemispherical contour was added to the interior of the inlet nozzle end section. The quarter-scale model does not have this feature. This change was made to strengthen the vessel and relieve the stress concentration.
2. The hemispherical contour on the outside of the end having the sapphire viewing ports was replaced with a bevel. This was to reduce the machining costs.
3. The nozzles were redesigned to furnish a wave ring seal in place of a brazed joint. This eliminated a material problem and strengthened the vessel.
4. The thread coupling for joining the vessel section was made larger to withstand autofrettage pressure of 0.67 GPa (98 ksi). The proposed manufacturer has no way of restraining the vessel for autofrettage.

Discussion

Stress corrosion cracking (SCC) studies and material evaluations are still in progress. The second 30-day test was conducted at University of Arizona to evaluate metallurgical specimens and materials when the water-filled vessel was subjected to a temperature of 343°C and a pressure of 0.2 GPa. The metallurgical prestressed and precracked specimens, which showed no crack growth from external examination, will be broken open and again examined for SCC. Visual examination of the optical surface of a synthetic sapphire and high alumina ceramics revealed surface etching and deterioration. The ceramic parts and the sapphire windows will probably have to be replaced periodically. The sapphire optical surface can be refinished, so the windows can be used again.

A fracture toughness analysis was made of the pressure vessel. The test condition of 0.4 GPa (58 ksi) in the vessel produces a maximum equivalent stress of 0.9 GPa (136.5 ksi) in the vessel. Using a fracture toughness value of 120 ksi $\sqrt{in}$ for the alloy steel, the critical crack length is 22.4 mm. This means that any crack or defect less than 22.4 mm in length will not propagate or cause failure in the vessel during testing.

Sandia-designed optical sapphire windows have been procured. A test fixture has been built for testing the windows to a pressure of approximately 276 MPa (40 ksi). The truncate-cone-shaped sapphire window has a major and a minor diameter of 57.1 mm and 38.1 mm, respectively, with a thickness of 27.77 mm. An annealed 0.254-mm copper gasket is used to help distribute the load and help make the joint seal (Figure 27). A more elaborate fixture may be built later to simulate the proof test pressure of 0.4 GPa (58 ksi) and temperature of 343°C. An existing pressure vessel will be used for this scheduled test.

An electric feedthrough has been designed for insertion from inside both the full-scale and the quarter-scale vessel (Figure 28). This design entails brazing the Kovar connector body to the alumina ceramic insulator and brazing molybdenum connector pins to the insulator. The connector base is a truncated cone, which is preloaded against the vessel and separated from it by a copper gasket. The vessel internal pressure is used to seal the joint; the higher the pressure, the tighter the seal. This same principle is used for such other joint seals as wave rings and sapphire windows. Ultrasonic specifications for nondestructive testing requirements are being formulated. Calibration blocks equal to the vessel wall thickness of 152.44 mm have been made of vessel material (Nationalloy, grade 7). These blocks will have holes (flaws) placed at various depths. These holes will be observed by using ultrasonic sensors. A final acceptance criterion will then be established for vessel procurement.

A quarter-scale vessel without center section (Figure 29) is now being built. Scaling is not perfect, but is sufficient to verify such critical design features as wall thickness, nozzles, coupling, and joints. This vessel will also be used to verify the critical process of autofrettage, which will require pressure of 676 MPa (98 ksi). This process, which will yield one-third of the inner-wall thickness, will make the vessel safer to use and should inhibit SCC. A finite-element stress analysis has been made to study the elastic and plastic stresses involved in autofrettage for verification of the required pressure. After autofrettage the vessel will be finish machined to final configuration. Then the completed assembly will be proof tested at a pressure of 0.4 GPa (58 ksi) and at ambient temperature. Strain gauge data will be collected during all pressure testing. The final test, to be made at University of Arizona, will be at 343°C and a pressure of 0.2 GPa (30 ksi). This is a functional test to determine the effects of temperature.

Final specifications and drawings that define the vessel design should be complete within 2 or 3 months, and vessel procurement can be made when funds become available.

Vessel Specifications:
Inside Diameter - 0.305 m
Outside Diameter - 0.610 m
Overall Length - 3.747 m
Total Weight - 6762 kg

Operating Conditions:
Temperature - Room to 343.3°C
Pressure - 1.014×10^5 Pa to 2.068×10^8 Pa

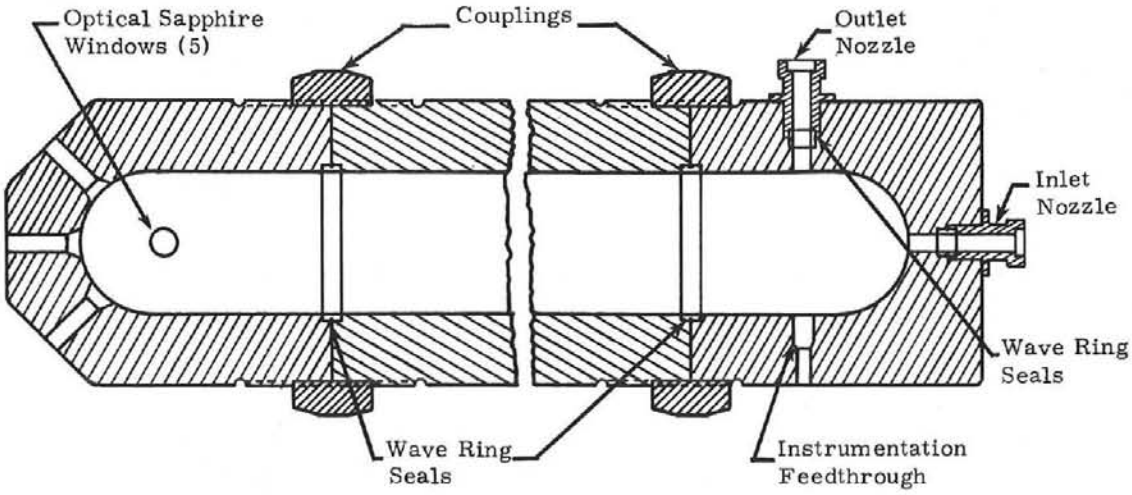

Figure 26. Environmental Test Vessel

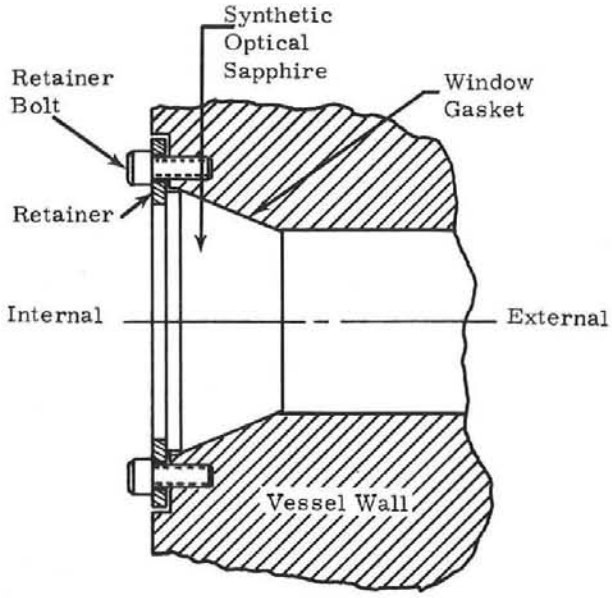

Figure 27. Sapphire Window

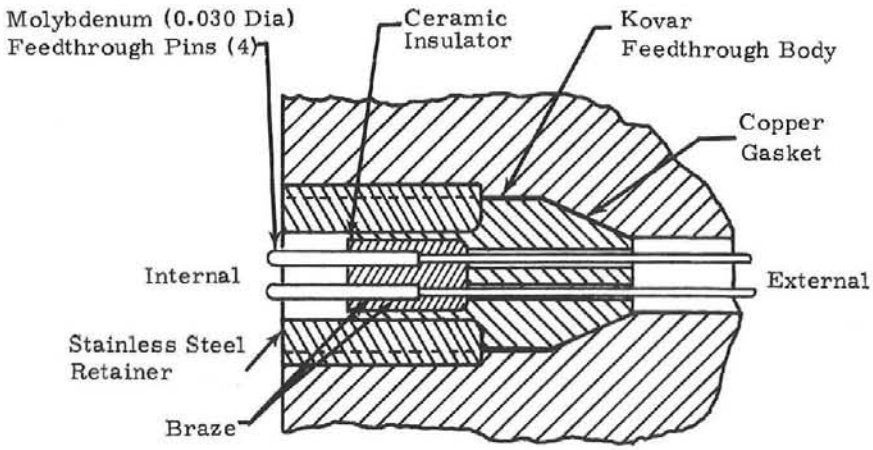

Figure 28. Quarter-Scale Vessel Instrumentation Feedthrough

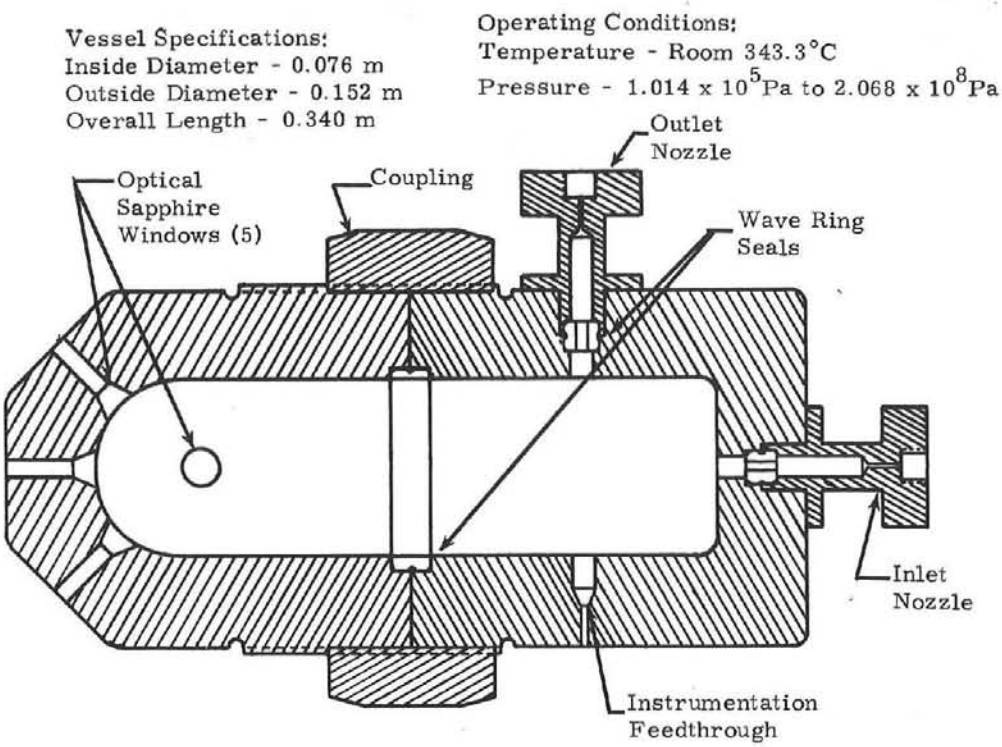

Figure 29. Quarter-Scale Environmental Test Vessel

Chapter 8

MAJOR LABORATORY EQUIPMENT ADDITIONS

Rock Saw

We have been sawing large rocks into laboratory-manageable sizes and have slabbed experimentally drilled rocks by the use of a walking-beam type of diamond saw. The method was so time consuming that it resulted in large expenditures for cutting rocks; therefore, a better method was needed. Efforts were made to locate a local stone cutter to do the work, but none with the required capability was found in the State.

A search of the rock-saw literature was made, and discussions were held with local stone cutters to determine what type of saw would work best for us. The decision was then made to purchase a diamond wire saw manufactured by W. J. Savage Co., Inc., of Knoxville, Tennessee. It has the capability of sawing a rock 1.7 by 4 m in cross section.

The saw has been delivered to Sandia and scheduled for installation by March 1, 1976.

Pressure Pump

A Partek Model 106X ES pump was purchased for use in conjunction with spark drilling experiments. The pressures that are generated by this pump are comparable to those used in actual drilling. The pump will be used extensively in the fluid jet and cavitation experiments.

Chapter 9

FACILITIES

Plans have been made to move our drilling laboratory into Bldg. 851. This building is currently in the extreme northeast side of Tech Area I; however, when the move (estimated to be done by March) is made, Tech Area boundaries will be changed so that the building will be outside the secure area and therefore accessible to visitors. The rock saw will be located adjacent to this building.

The staff members of the spark drilling team will be moved into our present personnel building. This move will bring us closer to the laboratory and also more accessible to visitors, as it is located outside the Tech Area.

These moves will interrupt our work somewhat, but no long delays are expected.

References

1. E. A. Martin, "Experimental Investigation of a High-Energy Density, High-Pressure Arc Plasma," J. Appl. Phys. 31, 255 (1960).

2. K. A. Naugolnykh et al., Electrical Discharges in Water. A Hydrodynamic Description, AD/A-00728, Foreign Technology Division, Wright-Patterson AFB, Ohio (December 1974).

3. R. H. Plumlee, Physical Processes in Liquid Switches, Sandia Laboratories Research Report SC-4469-355 (June 1969).

4. J. C. Martin, Duration of the Resistive Phase and Inductance of Spark Channels, SSWA/JCM/1065/25, unpublished.

5. A. Von Hippel, Dielectric Materials and Applications (The Technology Press of MIT, Wiley, 1954), V. 6.

6. R. C. O'Rourke, Note on Cylindrical and Plane Parallel Spark Channel, MLT 5-69, unpublished.

7. Yu Skvortsev, V. S. Komel'kov, N. M. Kuznetsov, "Expansion of a Spark Channel in a Liquid," Zhurnal Tekhnicheskoi Fisiki, Vol. 30, No. 10 (October 1960).

8. J. Handin, and M. Friedman, Fifth Quarterly Progress Report, dated October 15, 1975 for Sandia Laboratories Contract No. 82-9473.

DISTRIBUTION:

US Energy Res. and Dev. Admin. (25)
Division of Geothermal Energy
Washington, DC 20545
Attn: E. H. Willis, Director
R. Toms
M. Skalka
L. Bell
C. Carwile (20)
J. C. Bresee

US Energy Res. and Dev. Admin
Asst Administrator for Fossil Energy
Washington, DC 20545
Attn: Dr. P. White

US Energy Res. and Dev. Admin. (2)
Division of Oil Gas and Shale Technology
Washington, DC 20545
Attn: D. Guier
E. P. Ferrero

US Energy Res. and Dev. Admin. (2)
Albuquerque Operations Office
P.O. Box 5400
Albuquerque, NM 87115
Attn: H. E. Roser
D. K. Nowlin

US Energy Res. and Dev. Admin.
Sandia Area Office
P.O. Box 5400
Albuquerque, NM 87115
Attn: R. R. Malone

US Energy Res. and Dev. Admin.
Division of Physical Research
Washington, DC 20545
Attn: G. A. Kolstad

J. L. Lummus
Amoco Production Research
Research Center
P.O. Box 591
Tulsa, OK 74102

Thomas K. Perkins
Atlantic Richfield
R&D Department
P.O. Box 2819
Dallas, TX 75221

Joe K. Heilhecker
Exxon Production Research Co.
P.O. Box 2189
Houston, TX 77001

R. L. Parsons
Chevron Oil Field Research
Box 446
La Habra, CA 90631

Elard L. Haden
Continental Oil Company
Drawer 1267
Ponca City, OK 74601

H. A. Demirjian
Getty Oil Company
3903 Stoney Brook
Houston, TX 77042

Paul Berry
Mobil Research and Development
P.O. Box 900
Dallas, TX 75221

R. R. Angel
Phillips Petroleum Co.
450 FPB
Bartlesville, OK 74004

John D. Hellings
Shell Development Company
P.O. Box 481
Houston, TX 77001

W. C. Montgomery
Shell Development Company
P.O. Box 481
Houston, TX 77001

D. W. Clayton
Superior Oil Co.
P.O. Box 51108 O.C.S.
Lafayette, LA 70521

Dan Johnson Tenneco Oil Company
P.O. Box 2511
Houston, TX 77001

Thomas S. Teasdale
Texaco Research Laboratory
P.O. Box 425
Bellaire, TX 77401

H. H. Hasiba
Director, Production Division
Gulf Research & Development Co.
P.O. Drawer 2038
Pittsburg, PA 15230

W. C. Maurer (3)
Maurer Engineering
10301 Northwest Freeway
Suite 202
Houston, TX 77018

Sidney J. Green
Terra-Tek
University Research Park
420 Wakura Way
Salt Lake City, UT 84108

DISTRIBUTION (cont)

B. J. Livesay
Kennecott Exploration Inc.
10306 Roselle Street
San Diego, CA 92121

Joseph E. Zupanick
Sun Oil Company
503 N. Central Expressway
Richardson, TX 75080

William A. Glass
Big Chief Drilling Co.
Box 14837
Oklahoma City, OK 73114

Ray Marsh
Helmerich & Payne Int. Drilling Co.
P.O. Box 94968
Oklahoma City, OK 73109

W. J. Holbert
Rowan Drilling - U.S.
P.O. Box 1873
Midland, TX 79701

Robert F. Evans
Smith Tool
P.O. Box 15500
Irvine, CA 92705

W. F. Olson
Drilco Industrial
Box 3135
Midland, TX 79701

Chad L. Wiley
Reed Tool Company
P.O. Box 2119
Houston, TX 77001

Jim Kingsolver
Smith Tool
P.O. Box C-19511
Irvine, CA 92713

Roy M. Wolke
Oil Field Products Division
Dresser Industries, Inc.
P.O. Box 6504
Houston, TX 77005

Los Alamos Scientific Laboratory
P.O. 1663
Los Alamos, NM 87544
Attn: J. C. Rawley, Energy Division

National Science Foundation (2)
1800 G Street, NW
Washington, DC 20550
Attn: R. B. Coryell
W. Hakala

James F. Murray
General Electric Company
11177 E. Eight Mile Road
Detroit, MI 48232

Mahlon D. Dennis
General Electric Company
6325 Huntley Road
Worthington, OH 43085

Franklin D. Moore
Defense Communication Agency
Washington, DC 20305

Phillip Dodd
Division of Product & Materials Management
Grand Junction Office, ERDA
P.O. Box 2567
Grand Junction, CO 81501

Texas A&M University (2)
Center for Tectonophysics
College Station, TX 77843
Attn: M. Friedman
J. Handen, Dean of Geoscience

R. L. Whiting
Department of Petroleum Engineering
Texas A&M University
College Station, TX 77840

Albert Ellis
Professor of Applied Mechanics
University of California - San Diego
P.O. Box 109
La Jolla, CA 92037

E. L. McCandless
Union Carbide, Linde Division
270 Park Avenue
New York, NY 10017

H. D. Outmans
Union Oil Co. of California
Research Department
P.O. Box 76
Brea, CA 92621

DISTRIBUTION (cont)

1	M. Sparks
2	W. J. Howard
1000	G. A Fowler
1100	C. D. Broyles
1300	D. B. Shuster
1325	W. N. Caudle
2000	E. D. Reed
2100	W. J. Spencer
2150	C. M Tapp
2300	L. D. Smith
2320	K. L. Gillespie
2325	R. E. Fox
4010	C. Winter
5000	A. Narath
5160	W. Herrmann
5163	D. E. Munson
5700	J H. Scott
5710	G. E. Brandvold
5730	H. M. Stoller
5735	M. M. Newsom (50)
5740	V. L. Dugan
5742	S G Varnado
5800	R. S Claassen
5810	R. G. Kepler
5814	R. C. Hughes
5820	R. L. Schwoebel
5830	M. J. Davis
9400	H. E. Lenander
9412	R. K. Petersen
9414	G. L. Miller
8266	E. A. Aas (2)
3141	C. A. Pepmueller (Actg) (5)
3151	W. L. Garner (3)
	For ERDA/TIC (Unlimited Release)
ERDA/TIC (25)	
	(R.P. Campbell, 3171-1)